

# The properties of warm dark matter haloes

Mark R. Lovell,<sup>1★</sup> Carlos S. Frenk,<sup>1</sup> Vincent R. Eke,<sup>1</sup> Adrian Jenkins,<sup>1</sup> Liang Gao<sup>1,2</sup>  
and Tom Theuns<sup>1,3</sup>

<sup>1</sup>*Institute for Computational Cosmology, Durham University, South Road, Durham DH1 3LE, UK*

<sup>2</sup>*National Astronomical Observatories, Chinese Academy of Science, Beijing 100012, China*

<sup>3</sup>*Department of Physics, University of Antwerp, Groenenborgerlaan 171, B-2020 Antwerpen, Belgium*

Accepted 2013 December 13. Received 2013 December 13; in original form 2013 August 6

## ABSTRACT

Well-motivated elementary particle candidates for the dark matter, such as the sterile neutrino, behave as warm dark matter (WDM). For particle masses of the order of a keV, free streaming produces a cutoff in the linear fluctuation power spectrum at a scale corresponding to dwarf galaxies. We investigate the abundance and structure of WDM haloes and subhaloes on these scales using high resolution cosmological  $N$ -body simulations of galactic haloes of mass similar to the Milky Way's. On scales larger than the free-streaming cutoff, the initial conditions have the same power spectrum and phases as one of the cold dark matter (CDM) haloes previously simulated by Springel et al. as part of the Virgo consortium Aquarius project. We have simulated four haloes with WDM particle masses in the range 1.5–2.3 keV and, for one case, we have carried out further simulations at varying resolution.  $N$ -body simulations in which the power spectrum cutoff is resolved are known to undergo artificial fragmentation in filaments producing spurious clumps which, for small masses ( $<10^7 M_\odot$  in our case) outnumber genuine haloes. We have developed a robust algorithm to identify these spurious objects and remove them from our halo catalogues. We find that the WDM subhalo mass function is suppressed by well over an order magnitude relative to the CDM case for masses  $<10^9 M_\odot$ . Requiring that there should be at least as many subhaloes as there are observed satellites in the Milky Way leads to a conservative lower limit to the (thermal equivalent) WDM particle mass of  $\sim 1.5$  keV. WDM haloes and subhaloes have cuspy density distributions that are well described by Navarro–Frenk–White or Einasto profiles. Their central densities are lower for lower WDM particle masses and none of the models we have considered suffering from the ‘too big to fail’ problem recently highlighted by Boylan-Kolchin et al.

**Key words:** galaxies: dwarf – dark matter.

## 1 INTRODUCTION

The identity of the dark matter remains one of the central unsolved problems in cosmology. Various lines of evidence, for example, data on the cosmic microwave background radiation, indicate that the dark matter is made up of non-baryonic elementary particles (e.g. Larson et al. 2011), but exactly which kind (or kinds) of particles are involved is not yet known. For the past 30 years or so attention has focused on cold dark matter (CDM; see Frenk & White 2012 for a review), for which there are well-motivated candidates from particle physics, for example, the lightest supersymmetric particle or neutralino (Ellis et al. 1984), or the axion (Preskill, Wise & Wilczek 1983). CDM particles have negligible thermal velocities during the era of structure formation.

More recently, particle candidates that have appreciable thermal velocities at early times, and thus behave as warm, rather than cold, dark matter have received renewed attention. The best-known example is a sterile neutrino which, if it occurs as a triplet, could explain observed neutrino oscillation rates and baryogenesis (e.g. Asaka & Shaposhnikov 2005). This model is known as the neutrino minimal standard model ( $\nu$ MSM; Boyarsky, Ruchayskiy & Shaposhnikov 2009b; Boyarsky et al. 2009c); a list of alternative models may be found in Kusenko (2009). Warm particles are relativistic when they decouple from the primordial plasma and become non-relativistic during the radiation-dominated era. This causes the particles to freely stream out of small perturbations, giving rise to a cutoff in the linear matter power spectrum and an associated suppression of structure formation on small scales. When the particles collect at the centres of dark matter haloes, their non-negligible thermal velocities reduce their phase-space density compared to the CDM case and this can result in the formation of a ‘core’ in the

\* E-mail: [m.r.lovell@durham.ac.uk](mailto:m.r.lovell@durham.ac.uk)

density profile whose size varies inversely with the velocity dispersion of the halo (Hogan & Dalcanton 2000). However, recent analytical and numerical work (Macciò et al. 2012, 2013; Shao et al. 2013) has shown that the resulting cores are astrophysically uninteresting being, in particular, significantly smaller than the cores claimed to be present in dwarf satellites of the Milky Way (e.g. Gilmore et al. 2007; de Vega & Sanchez 2010).

On comoving scales much larger than the free-streaming cutoff, the formation of structure proceeds in very similar ways whether the dark matter is cold or warm and so current astronomical observations on those scales (larger than  $\sim 1$  Mpc) cannot distinguish between these two very different types of dark matter particles. Successes of the CDM paradigm, such as the remarkable agreement of its predictions (in a universe dominated by a constant vacuum energy,  $\Lambda$ ) with observations of temperature fluctuations in the cosmic microwave background radiation (e.g. Komatsu et al. 2011) and the clustering of galaxies (e.g. Cole et al. 2005), carry over, for the most part, to a warm dark matter (WDM) model. To distinguish between these two types of dark matter using astrophysical considerations it is necessary to resort to observations on the scale of the Local Group.

Over the past decade, surveys such as SDSS (York et al. 2000), PAndAS (Ibata et al. 2007) and Pan-STARRS (Kaiser et al. 2010) have begun to probe the Local Universe in detail. A number of new dwarf spheroidal (dSph) satellite galaxies have been discovered around the Milky Way and M31 (e.g. Willman et al. 2005; Walsh, Jerjen & Willman 2007; Martin et al. 2009, 2013; Bell, Slater & Martin 2011). Follow-up studies of stellar kinematics have been used to investigate their dynamics and mass content (Walker et al. 2009, 2010; Wolf et al. 2010; Tollerud et al. 2012). These data indicate that some dSphs have mass-to-light ratios of around 100, and are thus systems in which the properties of dark matter may be most directly accessible. Analyses of the number and structure of dSphs should therefore provide strong constraints on the nature of the dark matter.

The luminosity function of satellites in the Local Group has now been determined to quite faint magnitudes (Koposov et al. 2008; Tollerud et al. 2008), confirming that there are far fewer satellites around galaxies like the Milky Way than there are subhaloes in cosmological  $N$ -body simulations from CDM initial conditions (Diemand, Moore & Stadel 2005; Springel et al. 2005). This discrepancy is not new and can be readily explained by the physics of galaxy formation because feedback processes are very efficient at suppressing the formation of galaxies in small haloes (Bullock, Kravtsov & Weinberg 2000; Benson et al. 2002; Somerville 2002). Recent hydrodynamic simulations have confirmed this conclusion originally deduced from semi-analytical models of galaxy formation (Okamoto et al. 2010; Wadepuhl & Springel 2011).

Kinematical studies of the bright Milky Way satellites can constrain the internal structure of their dark matter subhaloes. Gilmore et al. (2007) argued that the data support the view that dSphs have central cores, in apparent contradiction with the results of  $N$ -body simulations which show that CDM haloes and their subhaloes have central cusps (Navarro, Frenk & White 1996b, 1997; Springel et al. 2005). Strigari, Frenk & White (2010) explicitly showed that it is always possible to find CDM subhaloes formed in the Aquarius high resolution simulations (HRS) of galactic haloes (Springel et al. 2008a) that are consistent with these data; however, the subhaloes that best fit the kinematical data for the bright satellites turn out *not* to be the most massive ones, as would naturally be expected for these bright satellites. This surprising result was explored in detail in the Aquarius simulations by Boylan-Kolchin, Bullock &

Kaplinghat (2011, 2012), who dubbed it the ‘too big to fail’ problem; it was also found in gas dynamic simulations of Aquarius haloes by Parry et al. (2012). The discrepancy has attracted a great deal of attention because it could potentially rule out the existence of CDM. Possibly related problems include the paucity of galaxies in voids (Tikhonov et al. 2009), and the local H I velocity width function (Zavala, Okamoto & Frenk 2008; Papastergis et al. 2011, but see Sawala et al. 2013).

A number of solutions to the ‘too big to fail’ problem have now been proposed. Within the CDM context, perhaps the simplest is that the virial mass of the Milky Way halo is smaller than the average mass,  $M_{200} \sim 1.4 \times 10^{12} M_{\odot}$ , of the Aquarius haloes (Wang et al. 2012; Vera-Ciro et al. 2013). A somewhat more uncertain possibility is that the central density of CDM subhaloes may have been reduced by the kind of explosive baryonic processes proposed by Navarro, Eke & Frenk (1996a) which appear to occur in some recent hydrodynamic simulations (Brooks & Zolotov 2012; Parry et al. 2012; Pontzen & Governato 2012; Zolotov et al. 2012) but not in others (di Cintio et al. 2011) which assume different prescriptions for physics that are not resolved in the simulations.

More radical solutions to the ‘too big to fail’ problem require abandoning CDM altogether. Vogelsberger, Zavala & Loeb (2012) show that simulations with a new class of ‘self-interacting’ dark matter could solve the problem. However, a solution is also possible with more conventional assumptions. In particular, Lovell et al. (2012) show that simulations with WDM produce very good agreement with the dSph kinematical data. The absence of small-scale power in the initial fluctuation field causes structure to form later than in the CDM case. Haloes of a given mass thus collapse when the mean density of the universe is smaller and, as a result, end up with lower central densities (Avila-Reese et al. 2001). However, the WDM model they assumed was ‘too warm’, in the sense that it assumed too low a particle mass (and thus too large a cut-off scale in the initial power spectrum) and produced only 18 dark matter subhaloes within 300 kpc of the main halo centre whereas observations suggest the actual number of satellites may be over an order of magnitude greater (Tollerud et al. 2008).

This constraint from subhalo central densities is one of several that can be used to place bounds on the WDM particle mass. The measured clustering of the Lyman  $\alpha$  forest lines at high redshift sets a lower limit to the particle mass (Viel et al. 2005; Boyarsky et al. 2009c; Viel et al. 2013) while the absence of X-rays from particle decay sets a (model dependent) upper limit to the mass of the sterile neutrino (whose decay rate into pairs of neutrinos and X-ray photons scales with the mass of the sterile neutrino; see Kusenko 2009; Boyarsky, Iakubovskiy & Ruchayskiy 2012, and references therein.)

The results of Lovell et al. (2012) and related results by Macciò et al. (2012, 2013) and Shao et al. (2013) raise the question of whether it is possible to find a range of WDM particle masses that lead to ‘warm enough’ models that match satellite central densities but which are also ‘cold enough’ to generate the observed number of satellite galaxies (Polisensky & Ricotti 2011; Kamada et al. 2013). In this work we examine both the number and structure of satellite galaxies in simulations as a function of the WDM particle mass.

The first requirement is to be able to count accurately the number of dark matter haloes formed in WDM cosmologies. The first simulations of WDM models (Bode, Ostriker & Turok 2001) showed the halo mass function to be suppressed as expected, but also found that at least 90 per cent of haloes, depending on the choice of power spectrum cutoff, formed from the fragmentation of filaments and had masses below the smoothing scale. Wang & White (2007)

examined this effect in hot dark matter (HDM) simulations (which assume a much larger power spectrum cutoff scale than in WDM) and showed that the fragmentation of filaments depends on the resolution of the simulation, thus concluding that most of the haloes in the Bode et al. (2001) simulations were due to a numerical artefact.

In this paper we introduce a series of methods for identifying spurious haloes in simulations, and then use our cleaned halo sample to examine the distribution and structure of WDM haloes as a function of the power spectrum cutoff. The paper is organized as follows. In Section 2 we present our simulation set and in Section 3 we describe our algorithm for removing spurious subhaloes. We then present our results in Section 4 and draw conclusions in Section 5.

## 2 THE SIMULATIONS

We begin by describing the details of our simulations, the procedure for generating initial conditions and a general overview.

### 2.1 Simulation parameters

Our  $N$ -body simulation suite is based upon that of the Aquarius Project (Springel et al. 2008a), a set of six (Aq-A through to Aq-F) galactic dark matter haloes simulated at varying resolution (levels 1-5, where level 1 corresponds to the highest resolution). The Aquarius simulations assumed cosmological parameter values derived from the *Wilkinson Microwave Anisotropy Probe* (WMAP) year 1 data. These have now been superseded and in this paper we use the cosmological parameter values derived from the WMAP year 7 data (Komatsu et al. 2011): matter density,  $\Omega_m = 0.272$ ; dark energy density,  $\Omega_\Lambda = 0.728$ ; Hubble parameter,  $h = 0.704$ ; spectral index,  $n_s = 0.967$ ; and power spectrum normalization  $\sigma_8 = 0.81$ .

Our main set of simulations follows the formation of four WDM galactic haloes with different effective WDM particle masses. The initial phases in the fluctuation spectrum are identical to those of the original CDM Aq-A halo but the transfer function is that appropriate to WDM as described below. In addition, we resimulated the level-2 Aq-A halo using the WMAP year-7 cosmology. For all five haloes (one CDM and four WDM), we ran simulations at different resolution. Our ‘high resolution’ suite corresponds to level 2 in the original Aquarius notation; it has particle mass of  $1.55 \times 10^4 M_\odot$ , and gravitational softening length of  $\epsilon = 68.1$  pc. All haloes were also run at ‘low resolution’ (level 4), with particle mass of  $4.43 \times 10^5 M_\odot$  and gravitational softening of  $\epsilon = 355.1$  pc. Finally, we ran an intermediate resolution version (level 3) of the WDM models with the lightest and heaviest dark matter particles, with particle mass  $5.54 \times 10^4 M_\odot$  and  $\epsilon = 125.0$  pc, in order to facilitate convergence studies. All haloes were simulated from  $z = 127$  to 0 using the GADGET3  $N$ -body code (Springel et al. 2008a).

To set up the initial conditions for the WDM runs we employed the transfer function,  $T(k)$ , defined as

$$P_{\text{WDM}}(k) = T^2(k)P_{\text{CDM}}(k), \quad (1)$$

where  $P(k)$  denotes the power spectrum as a function of comoving wavenumber  $k$ . We adopted the fitting formula for  $T(k)$  given by Bode et al. (2001):

$$T(k) = (1 + (\alpha k)^{2\nu})^{-5/\nu}, \quad (2)$$

where  $\nu$  and  $\alpha$  are constants. Bode et al. (2001) and Viel et al. (2005) find that  $\nu$  can take values between 1 and 1.2 depending on the fitting procedure; we adopted  $\nu = 1$  for simplicity. The position of the cutoff in the power spectrum is determined by the parameter  $\alpha$ , such that higher values of  $\alpha$  correspond to cutoffs at larger length-scales.

In principle, the initial conditions for WDM simulations should include thermal velocities for the particles (Colín, Valenzuela & Avila-Reese 2008; Macciò et al. 2012; Shao et al. 2013). However, at the resolution of our simulations, the appropriate velocities would have a negligible effect (Lovell et al. 2012) and are therefore not included. All of our CDM and WDM initial conditions employed a glass-like initial particle load (White 1994).

For our four WDM models we adopted values of  $\alpha$  of 0.0199, 0.0236 Mpc, 0.0297 and 0.0340  $h^{-1}$  Mpc, respectively. The last of these corresponds to the original WDM simulation presented in Lovell et al. (2012) which, however, assumed the WMAP year-1 cosmological parameters. That model was originally chosen as a thermal relic approximation to the M2L25 model of Boyarsky et al. (2009c), the  $\nu$ MSM parameter combination that has the largest effective free-streaming length that is still consistent with bounds from the Lyman  $\alpha$  forest (but see also Viel et al. 2013).

Bode et al. (2001) related  $\alpha$  to a generic thermal relic WDM particle mass,  $m_{\text{WDM}}$ , using the formula

$$\alpha = \frac{0.05}{h \text{ Mpc}^{-1}} \left( \frac{m_{\text{WDM}}}{1 \text{ keV}} \right)^{-1.15} \left( \frac{\Omega_{\text{WDM}}}{0.4} \right)^{0.15} \times \left( \frac{h}{0.65} \right)^{1.3} \left( \frac{g_{\text{WDM}}}{1.5} \right)^{-0.29}, \quad (3)$$

where  $\Omega_{\text{WDM}}$  is the WDM contribution to the density parameter; we have set the number of degrees of freedom,  $g_{\text{WDM}} = 1.5$ . We list the thermal relic masses for each of our models in Table 1, and use these masses as labels for the models, namely  $m_{2.3}$ ,  $m_{2.0}$ ,  $m_{1.6}$  and  $m_{1.5}$ ; we denote the CDM simulation with WMAP year-7 parameters as CDM-W7. We also give the cutoff mass scale for each simulation, which we define as the mass within a top hat filter which, when convolved with the CDM power spectrum, results in a function that peaks at the same value of  $k$  as the WDM power spectrum.

In order to compare our study to that of Viel et al. (2005, 2013) we need to take into account that the transfer function that we use assumes  $\nu = 1$  in equation (2) while theirs assumes  $\nu = 1.12$ . For values of  $k$  near the power spectrum cutoff, the transfer function for a given  $m_{\text{WDM}}$  has a higher amplitude if  $\nu = 1.12$  than if  $\nu = 1$ . To match the power on this scale then requires a higher value of  $m_{\text{WDM}}$  if  $\nu = 1$  than if  $\nu = 1.12$ . We can therefore derive an ‘equivalent  $\nu = 1.12$ ’ mass for each of our models which gives the best approximation to the transfer function in our  $\nu = 1$  simulations. These masses are listed in the final column in Table 1. [We carry out the comparison for  $T^2(k) > 0.5$  and use the equation relating  $m_{\text{WDM}}$  and  $\alpha$  given in equation 7 of Viel et al. 2005.]

The linear theory power spectra used to set up the initial conditions are plotted in Fig. 1. By construction, the peak of the power

**Table 1.** Parameters of the simulations. The parameter  $\alpha$  determines the power spectrum cutoff (equation 2);  $m_{\text{WDM}}$  is the thermal relic mass corresponding to each value of  $\alpha$ ; and  $M_{\text{th}}$  is the cutoff mass scale defined using a top hat filter as described in the text. The final column gives the particle masses that, when combined with the  $\nu = 1.12$  transfer function and  $m_{\text{WDM}}-\alpha$  relation of Viel et al. (2005), give the best approximation to our  $\nu = 1$  transfer functions.

Simulation	$m_{\text{WDM}}$ (keV)	$\alpha(h^{-1} \text{ Mpc})$	$M_{\text{th}}(M_\odot)$	$m_{\text{WDM}}^{\nu=1.12}$ (keV)
CDM-W7	–	0.0	–	–
$m_{2.3}$	2.322	0.01987	$1.4 \times 10^9$	1.770
$m_{2.0}$	2.001	0.02357	$1.8 \times 10^9$	1.555
$m_{1.6}$	1.637	0.02969	$3.5 \times 10^9$	1.265
$m_{1.5}$	1.456	0.03399	$5.3 \times 10^9$	1.106

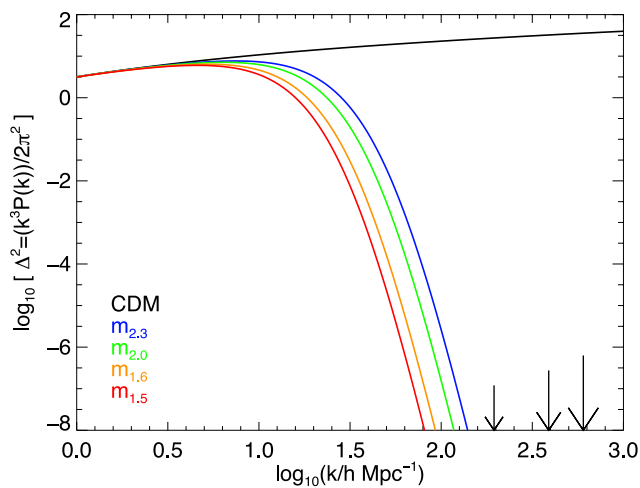


**Figure 1.** The linear theory power spectrum used in the simulations. The black line corresponds to the CDM model, CDM-W7, while the blue, green, orange and red lines correspond to the  $m_{2.3}$ ,  $m_{2.0}$ ,  $m_{1.6}$  and  $m_{1.5}$  WDM models, respectively. The arrows mark, in order of smallest to largest, the Nyquist frequency of our low, medium, and high resolution simulations.

spectrum moves to higher  $k$  as  $\alpha$  decreases (and the particle mass increases). For all WDM models the initial power spectrum peaks at a value of  $k$  smaller than the Nyquist frequency of the particle load in the simulation. This will lead to the formation of spurious halo as mentioned in Section 1.

Self-bound haloes were identified using the `SUBFIND` algorithm (Springel et al. 2001); they are required to contain at least 20 particles. The largest `SUBFIND` group is the galactic halo itself, to which we will refer as the ‘main halo’. Smaller haloes that reside within the main halo are known as ‘subhaloes’, whereas those that are outside the main halo are ‘independent haloes’. Most of the subhaloes will have experienced gravitational stripping whilst most of the independent haloes will have not.

A first view of the simulations is presented in Fig. 2. The smooth component of the main haloes is very similar in all five models: in all cases, the haloes are similarly centrally concentrated and elongated. The main difference is in the abundance of subhaloes. The myriad small subhaloes evident in CDM-W7 are mostly absent in the WDM models. For these, the number of subhaloes decreases as  $\alpha$  increases (and the WDM particle mass decreases).

The apparent similarity of the main haloes displayed in Fig. 2 is quantified in Table 2, which lists the masses and radii of the largest friends-of-friends halo in each simulation. The table gives their masses enclosed within radii of mean density 200 times the critical density ( $M_{200}$ ) and 200 times the background density ( $M_{200b}$ ). There is a slight trend of decreasing mass with increasing  $\alpha$ , but the maximum change is only 7 per cent for  $M_{200}$  and 2 per cent for  $M_{200b}$ . The change in cosmological parameters also makes only a small difference:  $M_{200}$  is 5 per cent higher for CDM-W7 than for the original Aquarius halo with *WMAP* year 1 parameters.

## 2.2 The structure of the main haloes

The density profiles of the main haloes (including substructures) in our HRS are plotted in Fig. 3. There is good agreement amongst all the haloes at radii (10–100) kpc, with the five profiles agreeing to better than 10 per cent. At larger radii, systematic differences between CDM-W7 and the WDM models begin to appear and these become increasingly pronounced for the warmer models. These

differences are due to slight variations in the position of large substructures in the outer parts. There are also small differences at much smaller radii (<10 kpc) which are not systematic and are thus likely due to stochastic variations in the inner regions.

The radial variation of the logarithmic slope of the density profile of each halo is plotted in Fig. 4. In all cases the slope at the innermost point plotted approaches the Navarro–Frenk–White (NFW) asymptotic value of  $-1$  but there is no evidence that the slope is converging. There is a slight tendency in the inner parts,  $r < 4$  kpc, for the slope in the WDM models to be shallower than in the CDM model, but there is no obvious trend with  $\alpha$ , possibly because of stochastic effects in the inner regions. Thus, apart from minor differences, the structure of these  $\sim 10^{12} M_{\odot}$  haloes varies little with power spectrum cut off, as expected for systems of mass  $\gg M_{\text{th}}$ .

## 3 REMOVAL OF SPURIOUS HALOES

One of the main aims of this study is to determine the mass function of subhaloes in WDM simulations. However, as we discussed in Section 1, simulations in which the initial power spectrum has a resolved frequency cutoff can undergo spurious fragmentation of filaments. An example is shown in Fig. 5, where we compare a region in one of our simulations with the corresponding region of a higher resolution simulation with the same initial conditions by plotting those particles that have collapsed into dark matter haloes. In both simulations there are two large haloes and several smaller ones. The large haloes have very similar sizes and positions in the two simulations, and can be regarded as genuine objects. By contrast, the small haloes have different sizes and positions in the two simulations; there are also more of them in the higher resolution case. As shown by Wang & White (2007), increasing the resolution even by rather large factors is not sufficient to prevent the formation of these artificial haloes. Using glass initial conditions, as we do for our simulations, does not reduce this problem. Future  $N$ -body codes that use phase space smoothing techniques may be able to alleviate this problem (Hahn, Abel & Kaehler 2012; Shandarin, Habib & Heitmann 2012; Angulo, Hahn & Abel 2013). At present, however, the only practical measure is to develop a reliable algorithm for identifying and removing these ‘spurious’ haloes from the halo catalogues.

We now introduce an algorithm for distinguishing between genuine and spurious subhaloes. It exploits three properties of the artefacts – mass, resolution dependence and the shape of the initial particle distribution – to define a series of cuts that isolate the artefacts. We present an outline of the method in Section 3.1 and provide details in Section 3.2. Note that while the results presented here have been derived for subhaloes that have been accreted into another halo, the algorithm is equally valid for independent haloes.

### 3.1 Outline of the methods

Previous simulations have shown that spurious haloes have small masses at formation and outnumber genuine haloes on those mass scales where they are present (Wang & White 2007). Thus, in principle, many spurious haloes can be singled out by applying a mass cut. This mass threshold, however, is not well defined because the mass function of genuine haloes overlaps that of the spurious haloes, so it is useful to introduce additional criteria to ensure that, as far as possible, all artificial haloes are identified and no genuine ones are removed.

The resolution dependence of the spurious fragmentation can be used to refine the distinction between genuine and artificial haloes.



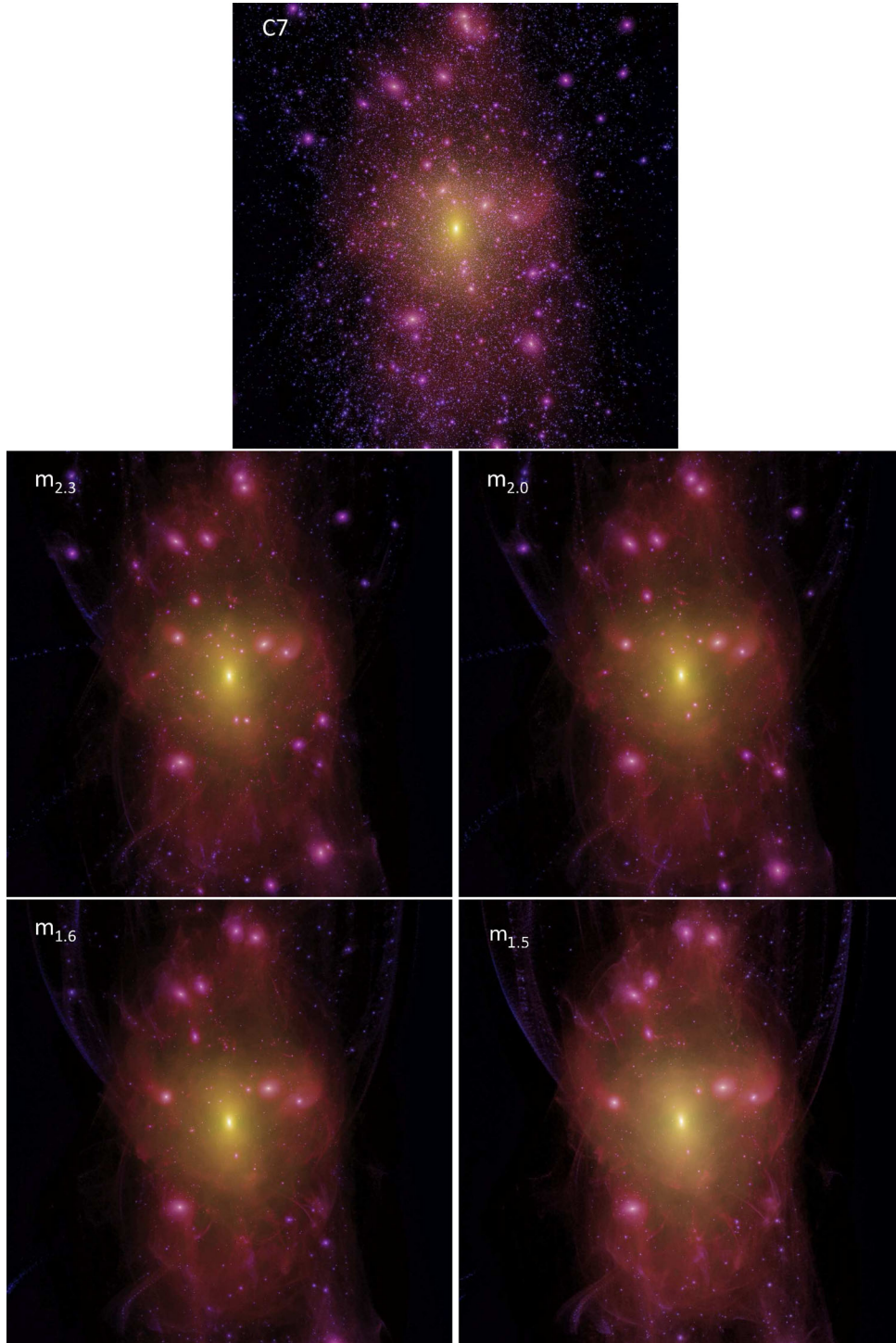


**Figure 2.** Images of our haloes at redshift  $z = 0$ . The panels show CDM-W7 (top),  $m_{2.3}$ ,  $m_{2.0}$ ,  $m_{1.6}$  and  $m_{1.5}$  (left to right, then top to bottom). The image intensity and hue indicate the projected squared dark matter density and the density-weighted mean velocity dispersion, respectively (Springel et al. 2008a). Each panel is 1.5 Mpc on a side.

While genuine haloes in a simulation at a given resolution are expected to be present in the same simulation at higher resolution, this need not be the case for spurious haloes, as illustrated in Fig. 5. Springel et al. (2008a) showed that it is possible to match haloes and subhaloes between different resolution simulations by tracing their particles back to the initial conditions and identifying overlapping Lagrangian patches in the two simulations. We refer

to the initial Lagrangian region of each halo, or more precisely the unperturbed simulation particle load, as its ‘protohalo’. The initial positions of the particles displayed in Fig. 5 are shown in Fig. 6. The two large objects originate from protohaloes of similar size and location, but there are clear discrepancies in the number, location and mass of the small objects. Thus, attempts to match small haloes in the two simulations will often fail because spurious

**Table 2.** Properties of the main friends-of-friends halo in each HRS. The radii  $r_{200}$  and  $r_{200b}$  enclose regions within which the mean density is 200 times the critical and background density, respectively. The masses  $M_{200}$  and  $M_{200b}$  are those contained within these radii. We also reproduce data from the original Aquarius Aq-A2 halo.

Simulation	$M_{200}(M_{\odot})$	$r_{200}(\text{kpc})$	$M_{200b}(M_{\odot})$	$r_{200b}(\text{kpc})$
CDM-W7	$1.94 \times 10^{12}$	256.1	$2.53 \times 10^{12}$	432.1
$m_{2.3}$	$1.87 \times 10^{12}$	253.4	$2.52 \times 10^{12}$	431.4
$m_{2.0}$	$1.84 \times 10^{12}$	251.7	$2.51 \times 10^{12}$	430.8
$m_{1.6}$	$1.80 \times 10^{12}$	250.1	$2.49 \times 10^{12}$	429.9
$m_{1.5}$	$1.80 \times 10^{12}$	249.8	$2.48 \times 10^{12}$	429.0
Aq-A2	$1.84 \times 10^{12}$	245.9	$2.52 \times 10^{12}$	433.5

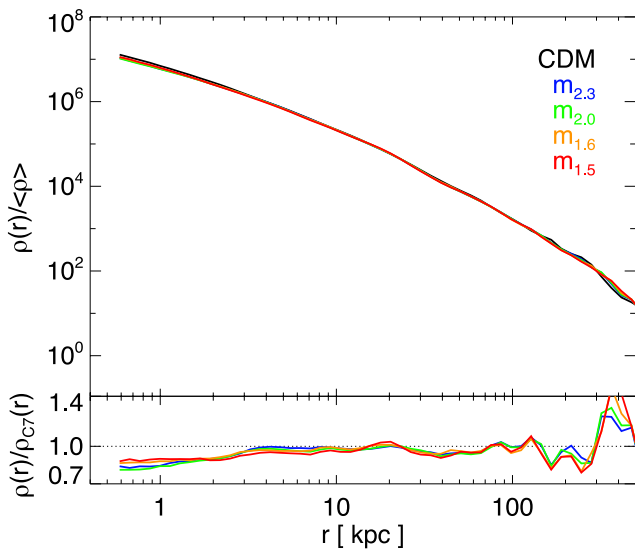


**Figure 3.** Density profiles of the main haloes (including subhaloes) in the simulations normalized by the background matter density. The line colours are as in Fig. 1. The profiles are plotted only beyond the ‘Power radius’ (Power et al. 2003) at which numerical convergence is expected. The bottom panel shows the profiles for the WDM simulations normalized to the profile for the CDM-W7 model.

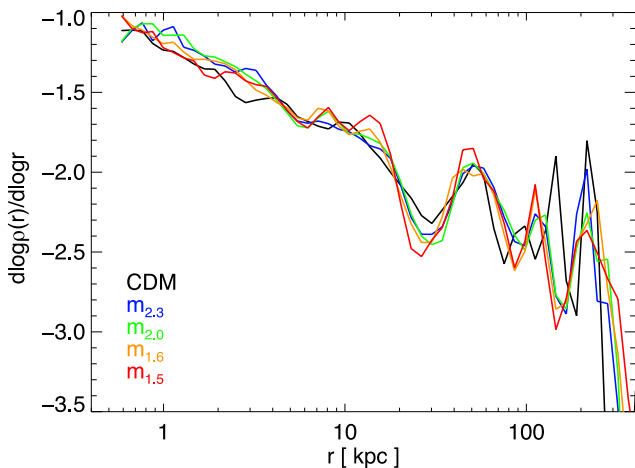


**Figure 4.** Radial variation of the logarithmic slope of the density profiles of the main haloes in the simulations. Line colours and plotting range are as in Fig. 3.

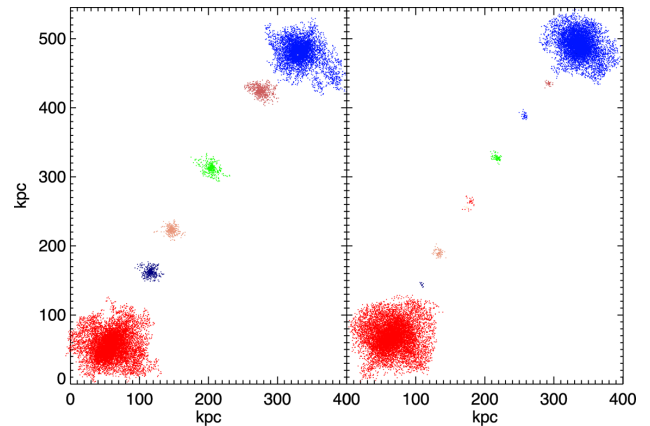


**Figure 5.** A region of a WDM simulation performed at two different resolutions. The particle mass for the HRS (right) is 29 times smaller than that of the low resolution case (left). Only particles in bound structures at this snapshot are shown. Particles are coloured according to the halo to which they belong. The number of particles plotted in each panel is equal to the number of bound-structure particles in the LRS; we have applied random sampling in the high resolution case.

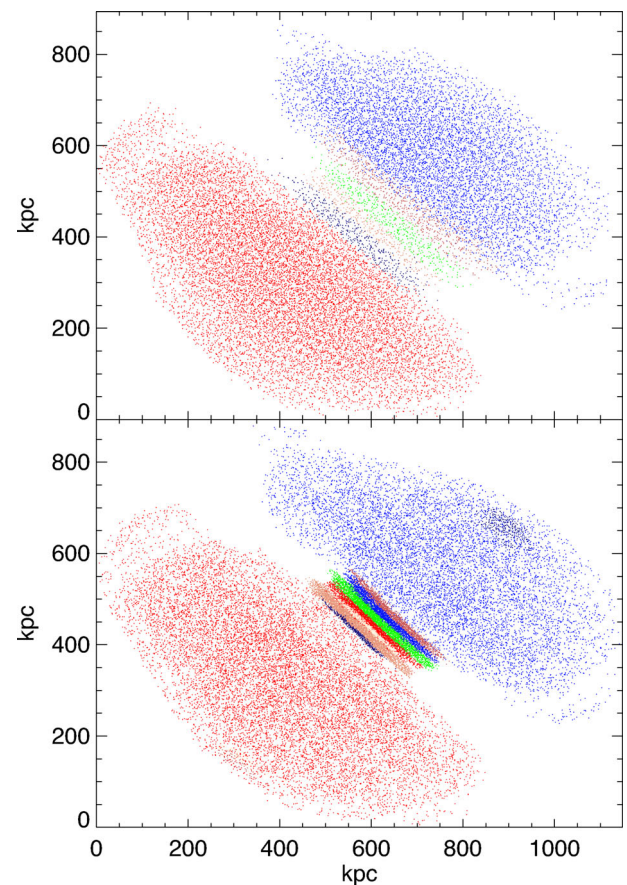


**Figure 6.** The particles of Fig. 5 traced back to their positions in the initial conditions. The LRS is shown in the top panel and the HRS in the bottom panel. Note the highly flattened configurations of spurious haloes.

haloes in the low resolution calculation do not have a counterpart in the HRS.

A third criterion exploits the most striking feature visible in Fig. 6: the shapes of the protohaloes. Genuine protohaloes are spheroidal,

whereas spurious protohaloes have much thinner, disc-like geometries. They can therefore be easily flagged as the progenitors of spurious haloes in the initial conditions.

In this study we are interested in objects that become subhaloes at the present day. We will apply these three criteria to them in the following order. First, we identify a cut based on protohalo shape, rejecting from the catalogue all subhaloes flatter than a given threshold. Secondly, we apply a mass cut; finally, we refine the mass cut using a matching procedure between simulations at different resolution. In what follows, we restrict attention to subhaloes lying within  $r_{200b}$  of the main halo centre at  $z = 0$  except where we state otherwise.

## 3.2 Application

### 3.2.1 Protohalo shapes

To determine the flattening of protohaloes we consider all the particles that make up a subhalo at some epoch (determined below), find their positions in the unperturbed simulation particle load and calculate the inertia tensor of the particle set:

$$I_{ij} = \sum_{\text{all particles}} m(\delta_{ij}|\mathbf{x}|^2 - x_i x_j), \quad (4)$$

where  $\delta_{ij}$  is the Kronecker delta function,  $m$  is the particle mass and  $\mathbf{x}$  is the particle position relative to the protohalo centre of mass. We take  $a \geq b \geq c$  to be the axis lengths of the uniform, triaxial ellipsoid that has the same moment of inertia tensor as the protohalo. We can then calculate  $s = c/a$ , known as the sphericity. A disc-like (or, more rarely, needle-like) spurious subhalo will have a major axis (disc diameter,  $a$ ) much longer than its minor axis (disc thickness,  $c$ ), and thus a small value of  $s$ . Genuine subhaloes, on the other hand, are spheroidal and thus have higher values of  $s$ .

We now need to choose an appropriate epoch at which to identify the particles that make up the protohalo. This should be well before the subhalo has fallen into a larger halo, after which its outer particles will be stripped. We select the earliest simulation snapshot below which the halo mass is more than half the maximum mass, the ‘half-maximum mass snapshot’. The initial positions of the particles in the object at this time are used to evaluate the protohalo sphericity.

The distributions of  $s$  for the subhaloes that survive to  $z = 0$  in the CDM-W7 and  $m_{1.5}$  simulations are illustrated in Fig. 7, as a function of  $M_{\text{Max}}$ . The mean sphericity is shown as a solid line and the 98 per cent range is indicated by the dotted lines in each case. The figure reveals two regimes. For values of  $M_{\text{Max}} > 10^9 M_{\odot}$ , the sphericity distributions in the two simulations are consistent with each other. For lower masses the protohaloes in the  $m_{1.5}$  simulation are much flatter than in CDM-W7. This clear dichotomy suggests that most of the  $m_{1.5}$  subhaloes with  $M_{\text{Max}} > 10^9 M_{\odot}$  are genuine and most of those with  $M_{\text{Max}} < 10^8 M_{\odot}$  are spurious. We can use the CDM subhaloes to define a cut in protohalo sphericity above which WDM subhaloes are likely to be real. We find that 99 per cent of CDM subhaloes containing more than 100 particles at the half-maximum mass snapshot have protohaloes with sphericity greater than  $\sim 0.16$  (depending slightly on simulation resolution), which we denote  $s_{\text{cut}}$ . We exclude from our cleaned subhalo catalogue any WDM subhalo whose protohalo has sphericity less than  $s_{\text{cut}}$ , regardless of mass. This cut rejects between 86 per cent ( $m_{2.3}$ ) and 93 per cent ( $m_{1.5}$ ) of the WDM subhaloes as spurious. We have checked, as we show later, that the subhaloes rejected by this criterion do not have clear counterparts in pairs of simulations of

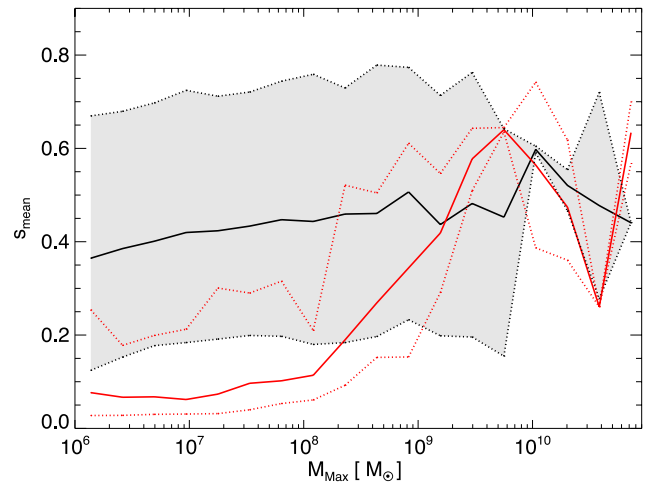


**Figure 7.** Mean subhalo sphericities as a function of  $M_{\text{Max}}$  for the high resolution CDM-W7 (black) and the  $m_{1.5}$  (red) runs. The region between the upper and lower 99 percentiles of the CDM distribution is shown in grey; the same region for the  $m_{1.5}$  simulation is delineated by the red dotted lines.

different resolution, where in this case the difference in resolution is a factor of 8. We find that varying  $s_{\text{cut}}$  by 20 per cent changes the number of subhaloes identified as genuine by less than 20 per cent, which is within the  $2\sigma$  Poisson uncertainty in the number identified using our chosen value of  $s_{\text{cut}}$ .

### 3.2.2 A first guess of the mass cut

For a first guess of the mass cut below which a majority of subhaloes are spurious, we resort to the results of Wang & White (2007). They showed that the characteristic mass below which spurious subhaloes begin to dominate the subhalo mass function is related to the matter power spectrum cutoff and the simulation resolution. The larger the value of the cutoff frequency and the higher the resolution of the simulation, the smaller is the mass of the largest spurious subhaloes. Wang & White (2007) derived an empirical formula for the mass at which spurious subhaloes begin to dominate:

$$M_{\text{lim}} = 10.1 \bar{\rho} d k_{\text{peak}}^{-2}, \quad (5)$$

where  $\bar{\rho}$  is the mean density of the Universe,  $d$  is the mean interparticle separation (a measure of resolution) and  $k_{\text{peak}}$  is the wavenumber at which the dimensionless power spectrum,  $\Delta^2(k)$ , has its greatest amplitude. We can apply this formula to  $M_{\text{Max}}$  to estimate a cut below which the majority of the subhaloes will be spurious. Some genuine haloes will have  $M_{\text{Max}}$  below this threshold but the mass limit can be refined using the matching criterion.

### 3.2.3 Matching subhaloes between simulations

A subhalo that is present in both a low resolution simulation (LRS) and in its high resolution counterpart (HRS) is likely to be genuine. We can use this property to refine the mass cut. We set the cutoff mass to be  $M_{\text{min}} = \kappa M_{\text{lim}}$ , where  $\kappa$  is a constant such that the number of LRS subhaloes of mass greater than  $M_{\text{min}}$  is equal to the number of subhaloes with matches in the HRS. We will assume that the value of  $\kappa$  determined for the LRS subhaloes is also applicable to the HRS catalogues.

We now introduce an algorithm for finding high resolution counterparts of the low resolution subhaloes. Genuine haloes should



originate from the same Lagrangian region regardless of resolution. Therefore, to match subhaloes we require a quantitative measure to compare these Lagrangian regions in simulations of different resolution and check that they overlap and have the same shape. These shapes are defined by point-like particles. In order to develop a quantitative measure of the overlap we need to smooth these points. We measure the degree to which a pair of objects in different resolution simulations are the ‘same’ by comparing the entirety of the regions from which they form. We introduce a statistic

$$R = \frac{U_{AB}^2}{U_{AA}U_{BB}}, \quad (6)$$

where  $U_{XY} = \int \phi_X \rho_Y dV$ ,  $V$  is volume, and  $\rho_{A/B}$  and  $\phi_{A/B}$  are the density of and gravitational potential due to the matter distributions A/B, respectively. It can be shown using Green’s Theorem that if the matter distribution of subhalo A is proportional everywhere to that of subhalo B,  $R = 1$ ; for any other configuration  $R < 1$ . We apply this formula to our candidate LRS–HRS protohalo particle distributions, representing each particle as a spherical shell of radius equal to the LRS mean interparticle separation and with infinitesimal thickness. The best match for the LRS subhalo will then be the HRS halo with which it attained the highest value of  $R$ . We retain this value of  $R$  for each LRS subhalo as our measure of its matching quality. A genuine LRS subhalo will have a good match at high resolution and therefore have a value of  $R$  close to 1, whereas a spurious subhalo will have a poor match and a lower value of  $R$ .

To find candidate matches, we first divide the simulation volume into a grid of cells of comoving length  $\gtrsim 60$  kpc, and, for a given low resolution protohalo, choose as candidate matches the high resolution protohaloes that occupy the same and neighbouring grid cells. It is computationally expensive to calculate  $R$  for the largest subhaloes, but we found that random sampling of each halo with 10 000 particles returned values of  $R$  that did not vary systematically with  $M_{\text{Max}}$  for subhaloes of  $M_{\text{Max}} > 10^9 M_\odot$ . We therefore adopt a threshold of 10 000 particles. When attempting to match subhaloes between simulations, minor differences in which particles are assigned to each subhalo can have an impact on  $R$ . We mitigate this problem by performing the calculation for both the maximum-mass and half-maximum mass snapshots, selecting the higher value of the two for each subhalo. The resulting values of  $R$  are plotted as a function of  $M_{\text{Max}}$  in Fig. 8.

At high masses, the CDM and WDM protohaloes have  $R$  close to 1. As the protohalo mass decreases,  $R$  becomes systematically lower and the decline is much steeper for the WDM models, as expected in the presence of poorly matching spurious subhaloes. Unfortunately, a small proportion of CDM subhaloes also attain low values of  $R$  and the demarcation between the distributions of  $R$  for WDM and CDM is much less clear cut than we found for the sphericity measurement,  $s$ . Were we to take the same approach for  $R$  as we did for  $s$ , we would infer a cut in  $R$  of about 0.68. More than half of the WDM subhaloes have a value of  $R$  closer to 1 than this, and since the sphericity-based algorithm rejects  $\sim 90$  per cent of subhaloes, adopting this cut in  $R$  would return a heavily contaminated sample. We circumvent this problem by using our sphericity cut to determine the distribution of  $R$  for spurious subhaloes. For each WDM model, we take 10 000 subsamples of 100 subhaloes that fail the sphericity cut (with replacement) and take the second highest  $R$  of each subsample to be the threshold,  $R_{\text{min}}$ , below which subhaloes are spurious. This result is not sensitive to the size of our subsamples. The mean value of  $R_{\text{min}}$  across the 10 000 subsamples is found to be in the range 0.94–0.96 for each of the four WDM models. For those subhaloes that instead pass the sphericity cut, the

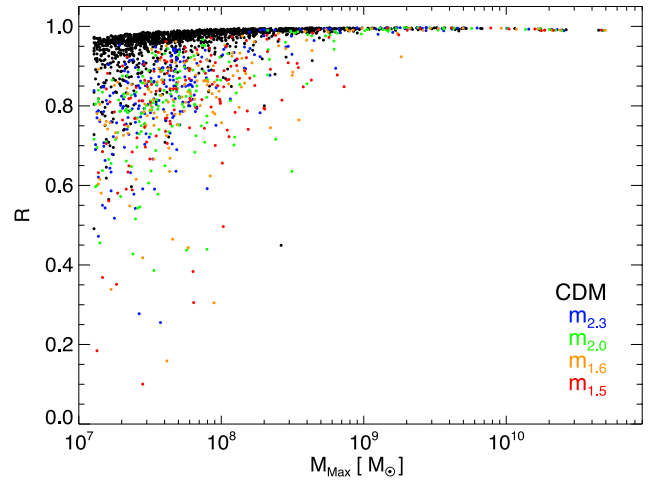


**Figure 8.**  $R$  as a function of  $M_{\text{Max}}$  for CDM and WDM LRS subhaloes matched to HRS counterparts (those that fail the sphericity cut are still included). The black dots denote CDM subhaloes, blue  $m_{2,3}$ , green  $m_{2,0}$ , orange  $m_{1,6}$  and red  $m_{1,5}$  (the same as Fig. 1).

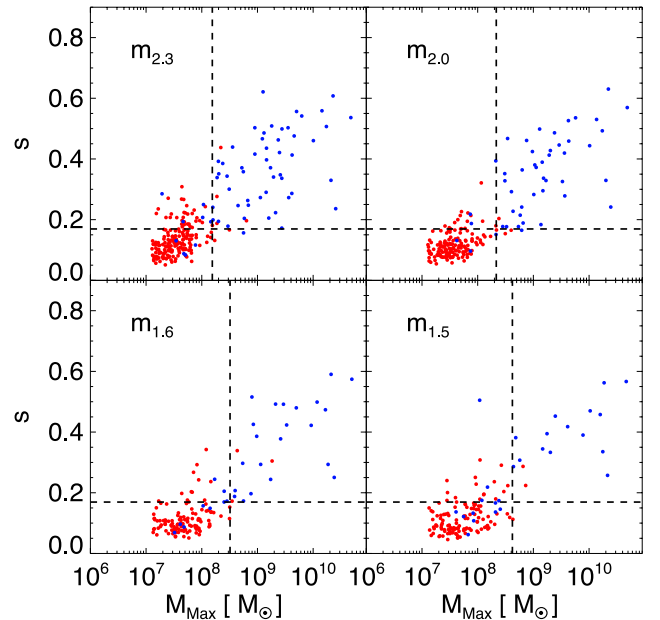


**Figure 9.** Dot plots of  $s$  and  $M_{\text{Max}}$  for subhaloes in the four different WDM models at low resolution. Blue points correspond to  $R \geq 0.94$  and red points to  $R < 0.94$ . The horizontal, dashed line is  $s_{\text{cut}}$  and the vertical line is  $M_{\text{min}}$ . All subhaloes are within  $r_{200b}$  of the main subhalo centre at redshift zero.

mean value of  $R_{\text{min}}$  is greater than 0.995 for all four models, showing that sphericity is a robust and accurate diagnostic of whether or not an object is spurious.

We now couple the matching and sphericity criteria to determine the optimal cut in  $M_{\text{Max}}$ . In Fig. 9, we plot  $s$  as a function of  $M_{\text{Max}}$  for the LRS subhaloes in each of our four WDM models, indicating their matching quality by colour. We adopt  $R_{\text{min}} = 0.94$ . We restrict attention to subhaloes that pass the sphericity cut and take a mass limit  $M_{\text{min}} = \kappa M_{\text{lim}}$  such that the number of subhaloes with mass greater than  $M_{\text{min}}$  is equal to the number of subhaloes with  $R > R_{\text{min}}$ . In Fig. 9 this is equivalent to the number of red dots to the right of the mass cut being equal to the number of blue dots to the left. We find that this condition requires values of  $\kappa$  between 0.4 and 0.6, given



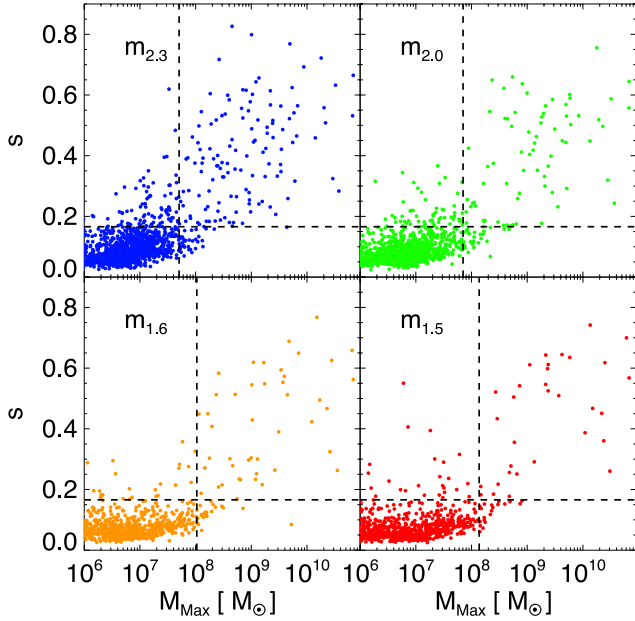


**Figure 10.** Dot plots of  $s$  and  $M_{\text{Max}}$  for subhaloes in the four different WDM models at high resolution. The horizontal, dashed line is  $s_{\text{cut}}$  and the vertical line is  $M_{\text{min}}$ . All subhaloes are within  $r_{200b}$  of the main subhalo centre at redshift zero.

the uncertainty in  $R_{\text{min}}$ . For simplicity, we will adopt  $\kappa = 0.5$ ; we find that this value provides a good compromise between rejecting low mass genuine objects and including high mass spurious subhaloes in all four models. Varying  $R_{\text{min}}$  and  $\kappa$  in the range stated here makes a difference of  $\sim 10$  per cent to the number of subhaloes returned in the  $m_{1,5}$  model and  $\sim 5$  per cent in the other cases. The values of  $M_{\text{min}}$  are then  $1.5 \times 10^8, 2.2 \times 10^8, 3.2 \times 10^8$  and  $4.2 \times 10^8 M_{\odot}$  for the  $m_{2,3}, m_{2,0}, m_{1,6}$  and  $m_{1,5}$  models, respectively, in the LRS. For the HRS, they decrease to  $5.1 \times 10^7, 7.0 \times 10^7, 1.1 \times 10^8$  and  $1.4 \times 10^8 M_{\odot}$ .

To summarize, we have used the mass, resolution dependent and Lagrangian region shape properties to identify spurious subhaloes in our subhalo catalogues. Having derived values for  $s_{\text{cut}}$  and  $M_{\text{min}}$  – the latter as a function of power spectrum cutoff and resolution – we can apply these cuts to the HRS. We plot the results in Fig. 10. Changing the value of  $\kappa$  in the range 0.4–0.6 produces a variation of  $< 5$  per cent in all four HRS models, and this does not affect our conclusions. In what follows we consider only those subhaloes that pass the cuts in each of these panels.

## 4 RESULTS

### 4.1 The subhalo mass and $V_{\text{max}}$ functions

In Fig. 11 we present the cumulative distributions of subhalo mass,  $M_{\text{sub}}$ , and  $V_{\text{max}}$  at  $z = 0$ , where  $V_{\text{max}}$  is defined as the peak amplitude of the circular velocity profile  $V_{\text{circ}} = \sqrt{GM(<r)}/r$ , with  $G$  being the gravitational constant and  $M(<r)$  the mass enclosed within radius  $r$ . This is a useful proxy for mass that is insensitive to the definition of the edge of the subhalo. The figure includes both genuine (solid lines) and spurious (dashed lines) subhaloes. Overall, the spurious subhaloes outnumber the genuine ones by a factor of 10. However, the mass function is dominated by genuine haloes beyond  $M_{\text{sub}} \sim (1-3) \times 10^7 M_{\odot}$ , corresponding to  $V_{\text{max}} \sim (4-6) \text{ km s}^{-1}$ , for the different models. The differential mass function (relative to the

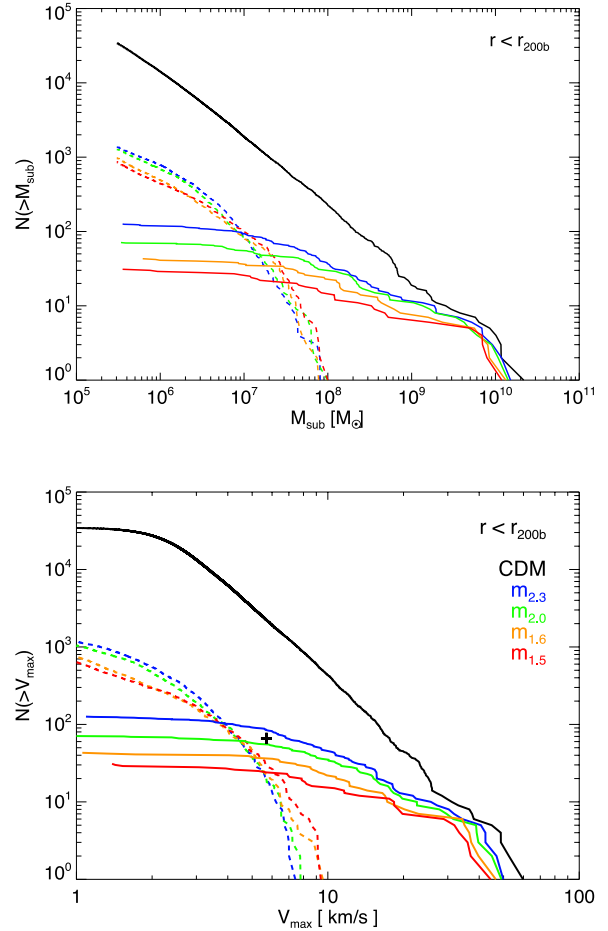


**Figure 11.** Cumulative subhalo mass,  $M_{\text{sub}}$  (top panel) and  $V_{\text{max}}$  (bottom panel) functions of subhaloes within  $r < r_{200b}$  of the main halo centre in the HRS at  $z = 0$ . Solid lines correspond to genuine subhaloes and dashed lines to spurious subhaloes. The black line shows results for CDM-W7 and the coloured lines for the WDM models, as in Fig. 1. The black cross in the lower panel indicates the expected number of satellites of  $V_{\text{max}} > 5.7 \text{ km s}^{-1}$  as derived in the text.

CDM mass function) for genuine haloes in the  $m_{2,3}$  case can be fitted with the functional form given by Schneider et al. (2012):

$$n_{\text{WDM}}/n_{\text{CDM}} = (1 + M_{\text{hm}}M^{-1})^{\beta}, \quad (7)$$

where  $M_{\text{hm}}$  is the mass associated with the scale at which the WDM matter power spectrum is suppressed by 50 per cent relative to the CDM power spectrum,  $M$  is subhalo mass and  $\beta$  is a free parameter. The best-fitting value is  $\beta$  of 1.3, slightly higher than the value of 1.16 found by Schneider et al. (2012) for friends-of-friends haloes (rather than `SUBFIND` subhaloes as in our case). A slightly better fit is obtained by introducing an additional parameter,  $\gamma$ , such that

$$n_{\text{WDM}}/n_{\text{CDM}} = (1 + \gamma M_{\text{hm}}M^{-1})^{\beta}, \quad (8)$$

with  $\gamma = 2.7$  and  $\beta = 0.99$ . However, better statistics are required to probe the subhalo mass function more precisely.

In principle, comparison of the abundance of subhaloes shown in Fig. 11 with the population of satellite galaxies observed in the Milky Way can set a strong constraint on the mass of viable WDM particle candidates. Assuming that every satellite possesses its own dark matter halo and that the parent halo in our simulations has a mass comparable to that of the Milky Way halo, a minimum requirement is that the number of subhaloes in the simulations above

some value of  $M_{\text{sub}}$  or  $V_{\text{max}}$  should exceed the number of Milky Way satellites above these values. In practice, the comparison is not straightforward because: (i) the values of  $M_{\text{sub}}$  or  $V_{\text{max}}$  for the observed population are not well known and (ii) the total number of Milky Way satellites is uncertain. Nevertheless, we can obtain a conservative limit on the mass of the particle as follows. There are 22 satellites in the Milky Way for which good quality kinematical data exist (Walker et al. 2009; Wolf et al. 2010). 11 of these are ‘classical satellites’ and the remainder are SDSS satellites. Of the classical satellites, eight are dSphs and the others are the large and small Magellanic clouds (LMC and SMC) and Sagittarius. Wolf et al. (2010) have estimated values of the mass (and line-of-sight velocity dispersion,  $\sigma_{\text{los}}^2$ ) within the (deprojected 3D) half-light radius for the eight classical and 11 SDSS dSphs. These are essentially insensitive to the velocity anisotropy of the stellar populations. The circular velocity within this radius is then given by

$$V_{\text{circ}}(r_{1/2}) = \sqrt{3\sigma_{\text{los}}^2}. \quad (9)$$

The values of  $V_{\text{circ}}$  are lower limits to  $V_{\text{max}}$  for each satellite. Leo IV has the smallest circular velocity,  $V_{\text{circ}} = 5.7 \pm 2.9 \text{ km s}^{-1}$ , of the 22 studied by Wolf et al. (2010). We show in Appendix A that our simulations have converged to better than 8 per cent at this value of  $V_{\text{max}}$ , showing that our conclusions are not affected by resolution issues (cf. Polisensky & Ricotti 2011). As shown by Springel et al. (2008b), values of  $V_{\text{max}}$  for subhaloes in Aquarius level 2 simulations are converged to within  $\sim 10$  per cent for  $V_{\text{max}} \geq 1.5 \text{ km s}^{-1}$ . We have examined the convergence in our  $m_{2.3}$  model and find that our L3 and L2 resolution  $V_{\text{max}}$  functions are converged to within  $2\sigma$  (Poisson) of each other for  $V_{\text{max}} > 4 \text{ km s}^{-1}$ . This is more modest than for the CDM Aquarius simulations, but sufficient to resolve the Leo IV type satellites. This result also gives us confidence that our ability to count satellites is not impaired by the numerical issues (cf. Polisensky & Ricotti 2011).

The known number of satellites in the Milky Way halo, 22, is a lower limit to the total number within 280 kpc of the galaxy’s centre, the distance to which the tip of the red giant branch can be detected in the SDSS. This is because although all the classical satellites (i.e. satellites brighter than  $M_V = -11$ ) have probably been discovered, SDSS surveyed only 20 per cent of the sky [data release 5 (DR5)]. Thus, a conservative lower limit to the WDM particle mass is obtained by requiring that the simulation should produce at least 22 satellites within this radius with  $V_{\text{max}} > 5.7 \text{ km s}^{-1}$ . Our  $m_{1.5}$  simulation produced only 25 subhaloes with  $V_{\text{max}}$  greater than this value within the larger radius,  $r_{200b} = 429 \text{ kpc}$ . Furthermore, the mass of the  $m_{1.5}$  halo,  $M_{200} = 1.80 \times 10^{12} M_{\odot}$ , is towards the higher end of acceptable values for the mass of the Milky halo; simulations of haloes with lower mass would produce even fewer subhaloes. Finally, any residual contamination by spurious subhaloes would artificially inflate the numbers in our subhalo sample. Thus, we can safely set a conservative lower limit to the mass of the WDM particle of  $m_{\text{WDM}} = 1.5 \text{ keV}$ .

We can set a less conservative but still robust lower limit to  $m_{\text{WDM}}$  by correcting the observed number of SDSS satellites to take into account the area surveyed. A simple extrapolation multiplying the observed number by a factor of 5 has to be taken with caution because we know that the classical satellites are not distributed isotropically but are concentrated towards a plane, called the ‘Great pancake’ by Libeskind et al. (2005). However, from analysis of the Aquarius simulations, Wang et al. (2012) have argued that such flat configurations occur only for the most massive  $\sim 10$  subhaloes and the anisotropy of the distribution falls off rapidly with increasing

sample size so that samples of  $\sim 50$  subhaloes follow quite close the overall shape of the halo. Based on this, we do not make any corrections for anisotropy and conclude that the Milky Way contains at least  $11 + 5 \times 11 = 66$  satellites with  $V_{\text{max}} > 5.7 \text{ km s}^{-1}$  within 280 kpc. Using the same argument as before, counting out to a radius of 419 kpc in the simulations to be conservative, we find that only the  $m_{2.3}$  and CDM models produces enough satellites to satisfy the limit.

To make an estimate of the halo-to-halo scatter, we make use of the result of Boylan-Kolchin et al. (2010) that the intrinsic scatter in the abundance of CDM subhaloes,  $\sigma_{\text{scatter}}$ , can be fitted by the sum of the Poisson,  $\sigma_p^2$ , and intrinsic,  $\sigma_i^2$ , variances

$$\sigma_{\text{scatter}}^2 = \sigma_p^2 + \sigma_i^2, \quad (10)$$

where  $\sigma_p^2 = \langle N \rangle$  and  $\sigma_i^2 = s_1 \langle N \rangle^2$ . Here,  $s_1$  is constant, which Boylan-Kolchin et al. (2010) calibrate against their simulation results and thus obtain  $s_1 = 0.18$ . They also found that the probability distribution for the number of subhaloes  $N$ , given the mean  $\langle N \rangle$  and intrinsic coefficient  $s_1$ , is well described by the negative binomial distribution:

$$P(N|r, p) = \frac{\Gamma(N+r)}{\Gamma(r)\Gamma(N+1)} p^r (1-p)^N, \quad (11)$$

where  $p = [1 + s_1^2 \langle N \rangle]^{-1}$  and  $r = s_1^{-2}$ . We then adopt the number of subhaloes within  $r_{200b}$  from each of our models as the distribution mean and compute the probability that a given halo will have at least 66 subhaloes. This probability equals 22 per cent for  $m_{2.0}$  and 0.30 per cent for  $m_{1.6}$ . Therefore, we conclude on this evidence that  $m_{\text{WDM}} > 1.6 \text{ keV}$ .<sup>1</sup> This is a more conservative limit than found by Polisensky & Ricotti (2011), although our choice of central halo is slightly more massive than theirs. A larger suite of WDM simulations is required to determine more precisely the variation in WDM subhalo abundance at a given host halo mass as well as the systematic variation of abundance with host halo mass.

#### 4.2 The radial distribution of subhaloes

The number density of subhaloes of mass  $M_{\text{sub}} > 10^8 M_{\odot}$  as a function of radius, normalized to the mean number density within  $r_{200b}$ , is shown in the top panel of Fig. 12. The bottom panel shows the cumulative number fraction of subhaloes per logarithmic radial interval. The number density profiles of subhaloes in the different WDM models are very similar to one another and to the CDM case. This uniformity is surprising since, as we shall see below, the central densities of WDM subhaloes decrease with decreasing WDM particle mass, making them increasingly vulnerable to tidal disruption. This result is reminiscent of that found by Springel et al. (2008a) that the number density profiles of Aquarius subhaloes are essentially independent of subhalo mass. It may be that better statistics might reveal differences in the radial distribution of WDM subhaloes.

The subhalo number density profiles are shallower than that of the halo dark matter. Springel et al. (2008a) found that the subhalo profiles are well described by an Einasto form (see equation 13 below), with  $r_{-2} = 199 \text{ kpc} = 0.81 r_{200}$  and  $\alpha_{\text{ein}} = 0.678$ . The lower panel of Fig. 12 shows that, as was the case for CDM, subhaloes lie

<sup>1</sup> check whether this limit is sensitive to our choice of  $s_{\text{cut}}$ , we repeated the analysis lowering  $s_{\text{cut}}$  by 20 per cent. In this case the probability for the  $m_{1.6}$  model increases to 2.7 per cent; thus this mass is still excluded at 95 per cent confidence.

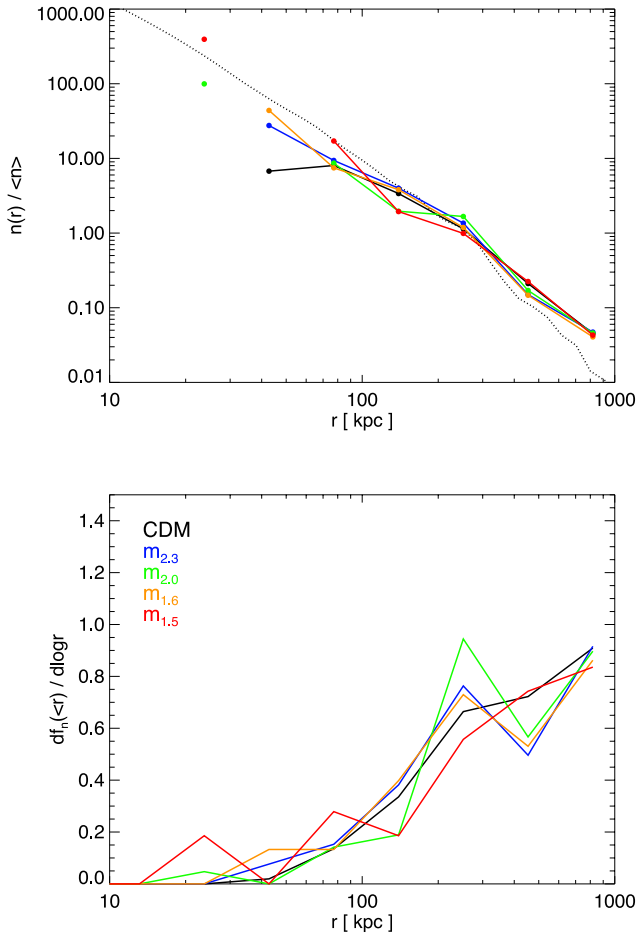


**Figure 12.** The radial distribution of subhaloes. Top: the spherically averaged number density of  $M_{\text{sub}} > 10^8 M_{\odot}$  subhaloes normalized to the mean overdensity at  $r_{200b}$  for our four WDM and one CDM models. The dotted line indicates the CDM main halo density profile from Fig. 3, renormalized to pass through the locus of radial distribution points at 250 kpc. Bottom: the number fraction of subhaloes per logarithmic interval in radius, on a linear log plot. The area under the curves is proportional to subhalo number, so this plot shows that subhaloes are preferentially found in the outer parts of the halo. The black line corresponds to the CDM model, CDM-W7, while the blue, green, orange and red lines correspond to the  $m_{2.3}$ ,  $m_{2.0}$ ,  $m_{1.6}$  and  $m_{1.5}$  WDM models, respectively.

preferentially in the outer parts of the halo, between 100 kpc and the virial radius, even though the number density is highest in the central regions.

The cumulative mass fraction in subhaloes as a function of radius is depicted in Fig. 13. As expected from the mass functions of Fig. 11, the subhalo mass fractions in the WDM models are lower than for CDM. At  $r_{200b}$ , the mass fractions in WDM subhaloes are approximately 5 per cent less than half the value in the CDM case. There is a small, but systematic decrease in the mass fraction with decreasing WDM particle mass.

### 4.3 The internal structure of WDM subhaloes

We now consider the internal structure of WDM haloes, particularly their radial density profiles. We begin by performing a convergence test of the profiles.

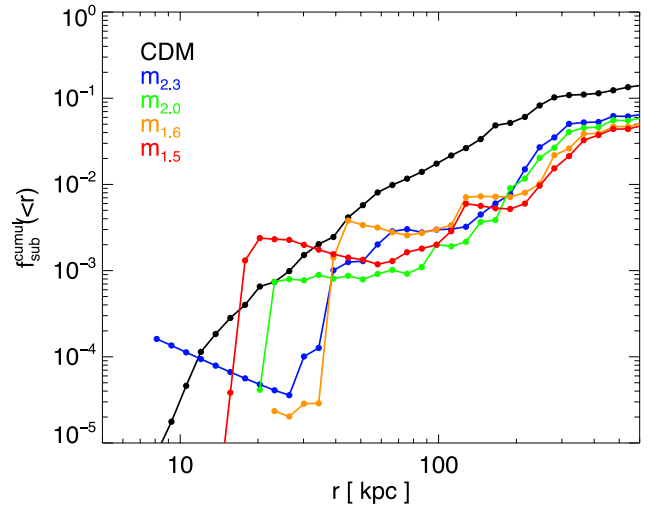


**Figure 13.** Cumulative mass fraction in substructures as a function of radius. The black line corresponds to the CDM model, CDM-W7, while the blue, green, orange and red lines correspond to the  $m_{2.3}$ ,  $m_{2.0}$ ,  $m_{1.6}$  and  $m_{1.5}$  WDM models, respectively.

#### 4.3.1 Convergence of the density profiles

Springel et al. (2008a) carried out a careful study of the convergence properties of the CDM Aquarius haloes upon which our set of WDM halo simulations is patterned. Here we carry out an analogous study of the WDM subhaloes. We focus on the most extreme case,  $m_{1.5}$ , since this differs most from CDM. Fig. 14 shows the density profiles of the nine most massive subhaloes lying within 500 kpc in the  $m_{1.5}$  simulation at three different resolutions (levels 2, 3 and 4). For the subhaloes of mass  $> 1 \times 10^9 M_{\odot}$ , we find that the three realizations agree extremely well at all radii satisfying the convergence criterion of Power et al. (2003). For those of lower mass, the low resolution (level 4) examples have fewer than 10 000 particles and although this limits the range where the convergence test is applicable, the convergence is still very good.

To emphasize the differences between subhaloes simulated at different resolution, we plot, in Fig. 15, the ratios of the intermediate and low resolution density profiles to that of their high resolution counterparts. At the smallest radius that satisfies the Power et al. (2003) criterion, the level 3 simulations are converged to better than 10 per cent; in most cases the same is true of the level 4 simulations. There are large excursions, however, in the outer parts, beyond  $\sim 10$  kpc. These are particularly noticeable for those subhaloes that are closer than 100 kpc from the main halo centre, and reflect the slightly different positions within the main halo of each of the matched subhaloes.

We can determine the mass range where the density profiles are converged by considering the ratio of circular velocities at the convergence radius of Power et al. (2003) between matched subhaloes at different resolution. Demanding that deviations from the level-2 simulation should not exceed 10 per cent, we find that the structure of level-3 subhaloes is well converged for subhalo masses  $> 10^8 M_{\odot}$  whereas for level-4 subhaloes convergence is only achieved for masses  $> 10^9 M_{\odot}$ .

#### 4.3.2 The density profiles of subhaloes

We now consider the spherically averaged radial density profiles of subhaloes in all four different WDM models. For the CDM case



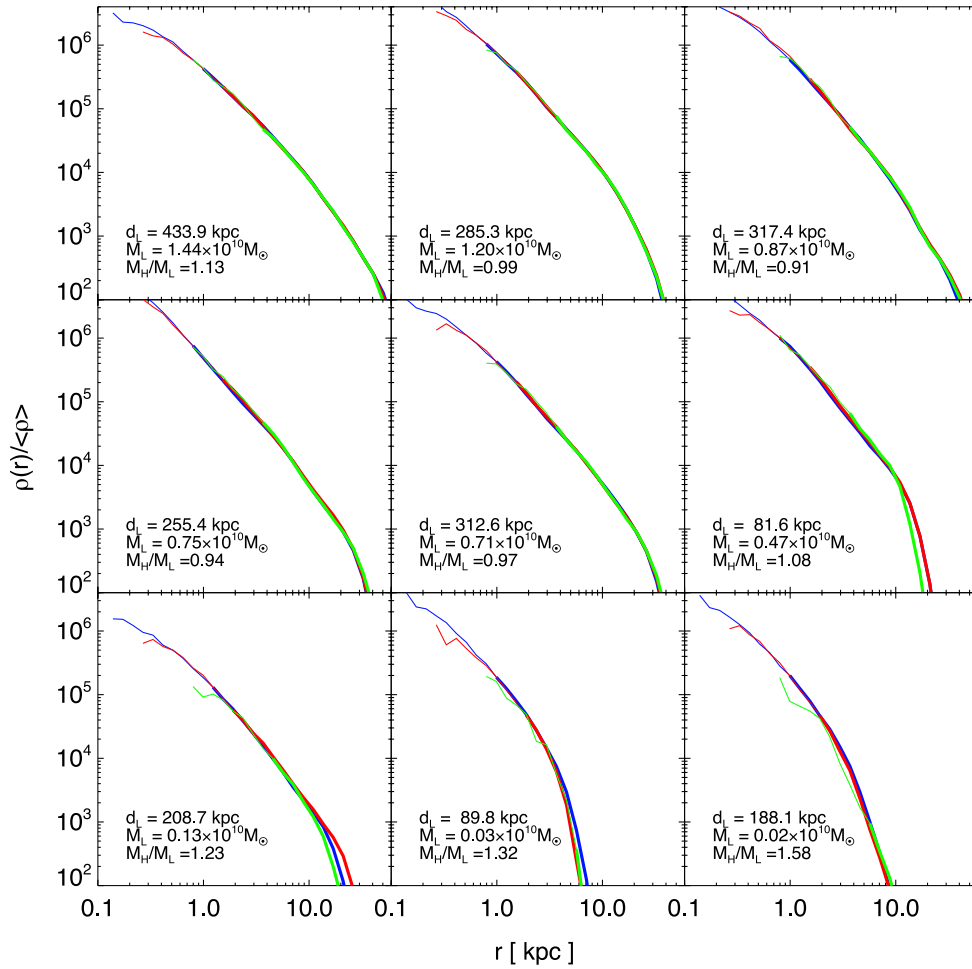


**Figure 14.** Spherically averaged radial density profiles for subhaloes matched between the high (level 2), intermediate (level 3) and low (level 4) resolution versions of the  $m_{1.5}$  simulation. Blue corresponds to high, red to intermediate and green to low resolution. The density profiles are shown by thick lines down to the smallest radius at which they satisfy the convergence criterion of Power et al. (2003), and are continued by thin lines down to a radius equal to twice the softening length. In the legend,  $d_L$  is the distance of the low resolution subhalo from the main halo centre,  $M_L$  is the subhalo mass and  $M_L/M_H$  is the ratio between the masses of the low and high resolution counterparts.

Springel et al. (2008a) found that the profiles of subhaloes are well fitted by either an NFW (Navarro et al. 1996b, 1997) or an Einasto (Einasto 1965; Navarro et al. 2004) functional form. The NFW profile is given by

$$\rho(r) = \frac{\delta_c \rho_{\text{crit}}}{(r/r_s)(r/r_s + 1)^2}, \quad (12)$$

where  $\delta_c$  is a characteristic overdensity (usually expressed in units of the critical density) and  $r_s$  is a spatial scale that marks the transition between the asymptotic slopes of  $-1$  and  $-3$ . The Einasto profile is given by

$$\rho(r) = \rho_{-2} \exp\left(-\frac{2}{\alpha_{\text{ein}}}\left[\left(\frac{r}{r_{-2}}\right)^{\alpha_{\text{ein}}} - 1\right]\right), \quad (13)$$

where  $r_{-2}$  is the scale (analogous to  $r_s$ ) where the profile attains a slope of  $-2$ ,  $\rho_{-2}$  is the density at  $r_{-2}$  and  $\alpha_{\text{ein}}$  is a shape parameter. Springel et al. find that Einasto fits (which have an additional free parameter) are marginally better than NFW fits for CDM subhaloes even when  $\alpha_{\text{ein}}$  is fixed to a constant.

Following Springel et al. (2008a) we define a goodness of fit statistic for the functional fits to the subhalo profiles as

$$Q^2 = \frac{1}{N_{\text{bins}}} \sum_i [\ln \rho_i - \ln \rho^{\text{model}}(r_i)]^2, \quad (14)$$

where  $\rho_i$  is the density measured at radius  $r_i$  and  $\rho^{\text{model}}$  is the model density evaluated at that same radius. In Fig. 16, we show how well our subhaloes can be fitted by NFW and Einasto profiles, in the latter case with fixed shape parameter ( $\alpha_{\text{ein}} = 0.18$ , following Springel et al. 2008a), by plotting the median value of  $Q$  for each of the different models as a function of the thermal equivalent WDM particle mass. As for CDM, we find that the Einasto profile is a marginally better fit to WDM subhaloes than the NFW profile. There is little variation in the quality of the Einasto fits for the different values of the particle mass, but the NFW fits seem to become slightly worse with increasing mass.

The density profiles of subhaloes vary systematically with the WDM particle mass. Before performing a statistical comparison, we illustrate this variation with a few examples of subhaloes that we have been able to match across simulations with different WDM particle masses. Such matches are not trivial because the subhaloes have masses close to the cutoff in the initial power spectrum and

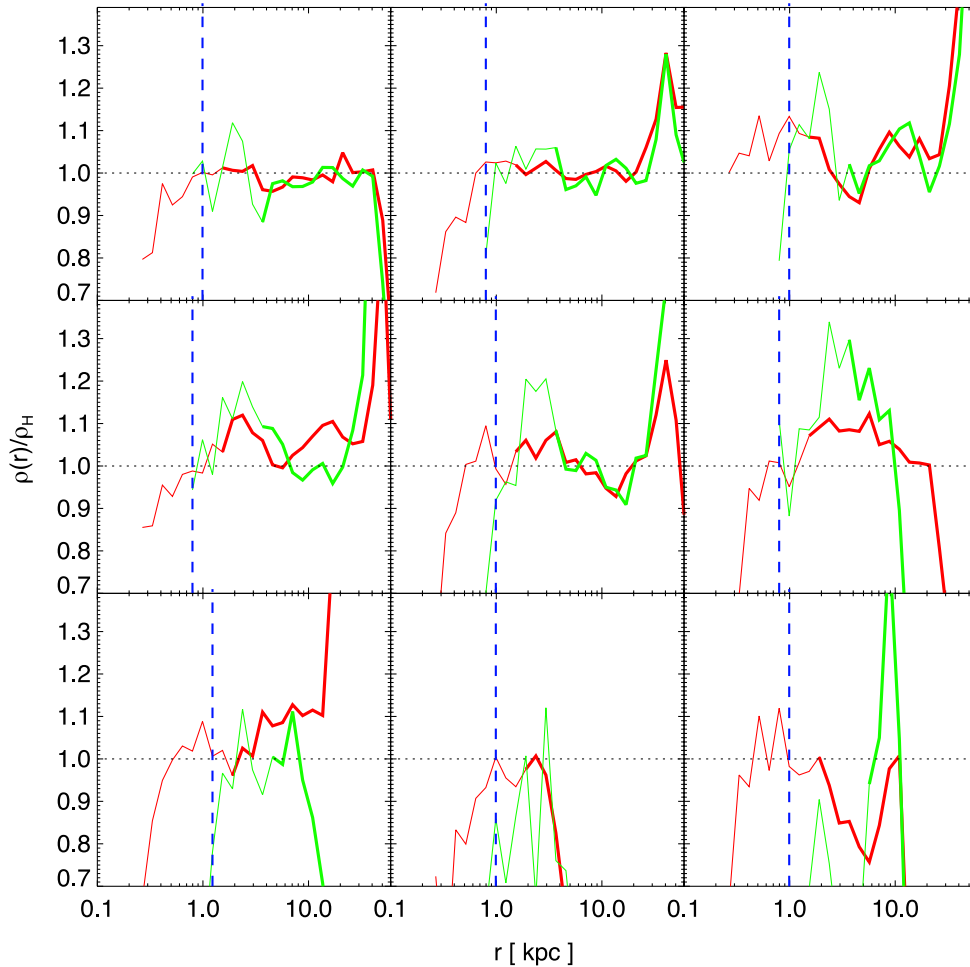


**Figure 15.** Ratio of the intermediate (level 3; red) and low (level 4; green) resolution density profiles of the  $m_{1.5}$  subhaloes shown in Fig. 14 to the density profile of their high resolution (level 2) counterparts. The blue dashed line indicates the convergence radius for the high resolution subhaloes.

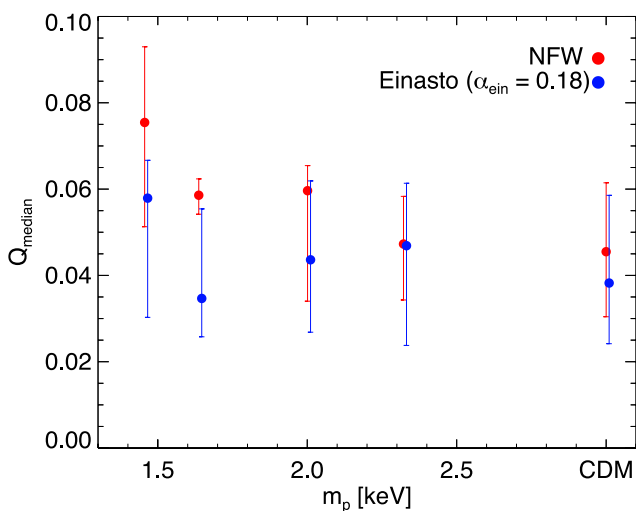


**Figure 16.** Median value of the goodness of fit statistic,  $Q$ , for Einasto (blue dots) and NFW (red dots) fits to all subhaloes of  $M_{\text{sub}} > 10^9 M_{\odot}$ , as a function of the WDM particle mass,  $m_{\text{WDM}}$ . In the Einasto fits, we have fixed  $\alpha_{\text{ein}} = 0.18$ . The error bars indicate the upper and lower quartiles of the distribution. The Einasto data points are slightly offset in  $m_{\text{WDM}}$  for clarity.

thus their formation histories can vary substantially from one case to another. In Fig. 17 we show nine examples of subhaloes where, based on their positions and masses, we have been able to identify likely matches. In Fig. 18, we show the ratio of the profiles to that of their CDM counterpart.

The differences amongst the profiles tend, in most cases, to be larger at smaller radii. As the WDM particle mass decreases, the subhalo profiles tend to become shallower. At the innermost converged point, the density of the subhalo with the smallest value of  $m_{\text{WDM}}$  is generally a factor of several smaller than its CDM counterpart. For example, the  $m_{1.5}$  keV subhalo in the central panel of the Figs 17 and 18 is a factor of  $\sim 3$  less dense at the innermost converged point than its CDM counterpart and a factor of  $\sim 2$  less dense than the subhalo with  $m_{2.3}$  keV.

The trends seen in Figs 17 and 18 reflect the fact that, for fixed cosmological parameters, haloes of a given mass form later in WDM models than in CDM (Avila-Reese et al. 2001; Lovell et al. 2012). We can quantify the difference by comparing, for example, the central masses of haloes in our various models. The masses enclosed within 300 pc and 2 kpc of the centre in field haloes and subhaloes in our simulations are plotted in Fig. 19 as a function of halo mass. For field haloes (left-hand panel) there is a clear separation at both radii amongst the different models: at fixed mass, the WDM haloes have lower central masses than their CDM-W7 counterparts and the enclosed mass decreases with the WDM particle mass. For (field)

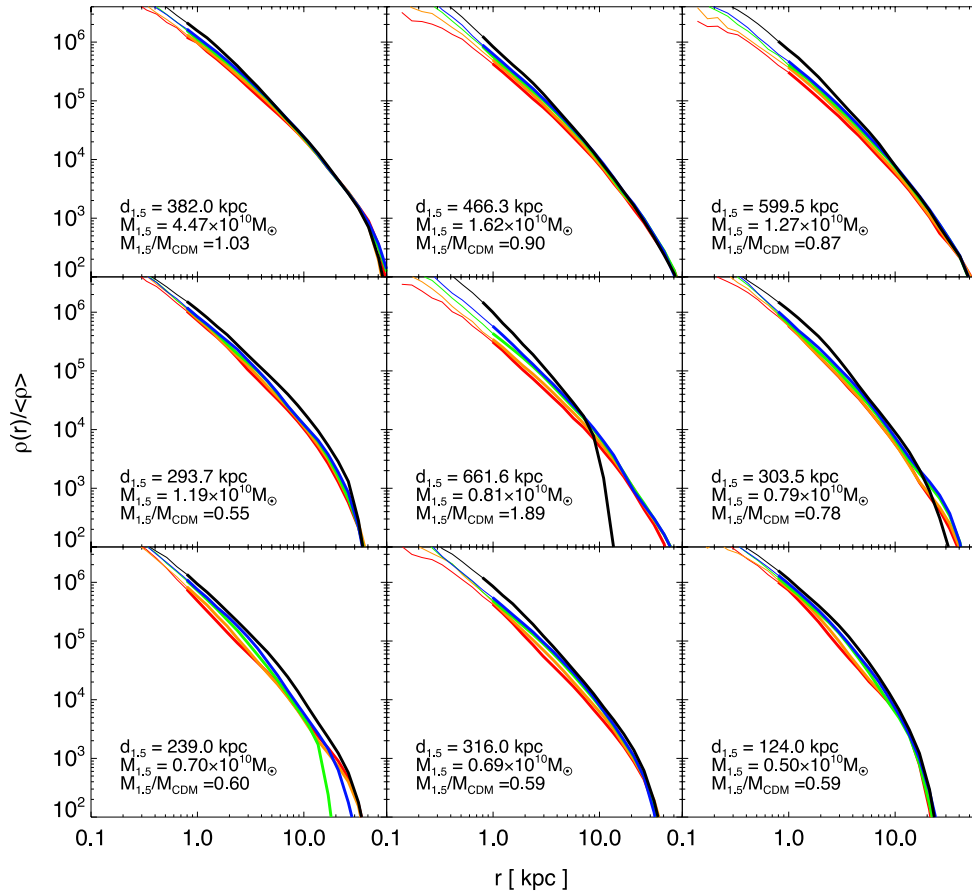


**Figure 17.** Spherically averaged radial density profiles of subhaloes in simulations of different WDM particle mass. The subhaloes have been matched across simulations on the basis of their position and mass. However, it should be noted that in some cases the matches are uncertain. The different colours correspond to different WDM particle masses: red, orange, green and blue to 1.5, 1.6, 2 and 2.3 keV, respectively, while black corresponds to the CDM case. In the legend,  $d_{1.5}$  is the distance of the subhalo from the main halo centre in the  $m_{\text{WDM}} = 1.5$  keV,  $M_{1.5}$  is the mass of the subhalo also in this case, and  $M_{1.5}/M_{\text{CDM}}$  is the ratio of this mass to that of the CDM counterpart. As in Fig. 14 the density profiles are shown by thick lines down to the smallest radius at which they satisfy the convergence criterion of Power et al. (2003), and are continued by thin lines down to a radius equal to twice the softening length.

haloes of mass less than  $5 \times 10^9 M_{\odot}$ , the masses enclosed within 300 pc are lower relative to the CDM case by factors of  $\sim 4$  and  $\sim 3$  in the  $m_{1.6}$  and  $m_{2.3}$  models, respectively. At higher masses the differences are smaller (by factors of 2 and 3 for the  $m_{2.3}$  and  $m_{1.6}$  cases, respectively), thus the main halo density profiles varies very little for this range of  $m_{\text{WDM}}$ . The situation is somewhat different for subhaloes (right-hand panel), largely because tidal stripping removes material from the outer regions, leaving the central density largely unaffected. As a result, after falling into their host halo, objects move primarily to the left in Fig. 19 but the change is comparatively greater for the less concentrated WDM subhaloes than for the CDM subhaloes. Nevertheless, an offset amongst the WDM subhaloes and amongst these and the CDM subhaloes remains, particularly at large masses.

Another measure of central mass is provided by the value of  $V_{\text{max}}$  which we plot as a function of mass for field haloes in Fig. 20. There is a marked difference between the CDM-W7 and the WDM haloes which, at a given mass, have a lower  $V_{\text{max}}$ . As expected, these differences decrease with increasing halo mass. At  $10^9 M_{\odot}$  the mean value of  $V_{\text{max}}$  for the  $m_{2.3}$  case is a factor of 1.33 smaller than for CDM-W7.

The differences in the internal structure of haloes in the WDM and CDM cases can be further quantified by comparing the relation between  $V_{\text{max}}$  and  $r_{\text{max}}$ , the radius at which  $V_{\text{max}}$  is attained. We plot

these relations separately for independent haloes and subhaloes in Fig. 21. Tidal stripping of CDM subhaloes causes their value of  $V_{\text{max}}$  to drop less rapidly than their value of  $r_{\text{max}}$ , leading to an increase in the concentration of the subhalo (Peñarrubia, McConnachie & Navarro 2008; Springel et al. 2008a). As may be seen by comparing the top and bottom panels of Fig. 21, the values of  $r_{\text{max}}$  for CDM subhaloes at fixed  $V_{\text{max}}$  are typically 70 per cent of the values for field haloes.<sup>2</sup> Since WDM subhaloes are less concentrated than their CDM counterparts to begin with, they are more susceptible to stripping once they become subhaloes (see also Knebe et al. 2002). Thus, at fixed  $V_{\text{max}}$ , the values of  $r_{\text{max}}$  in the  $m_{2.3}$  case are now typically only 40 per cent of the values for field haloes. Even so, since the typical values of  $r_{\text{max}}$  for subhaloes with  $V_{\text{max}} > 10 \text{ km s}^{-1}$  are greater than 1 kpc (even in the models with the smallest WDM particle mass), the majority of any dSphs residing in subhaloes like these would not show clear signs of tidal disruption.

<sup>2</sup> This number depends on the choice of cosmological parameters. For the Aquarius simulations (which assumed *WMAP1* cosmological parameters), this number decreases to 62 per cent (Springel et al. 2008a), as can be seen by comparing the dotted lines in the two panels of Fig. 20. This difference is driven primarily by the higher value of  $\sigma_8$  in the *WMAP1* cosmology which causes haloes of a given mass to collapse earlier and thus be more concentrated than their *WMAP7* counterparts.



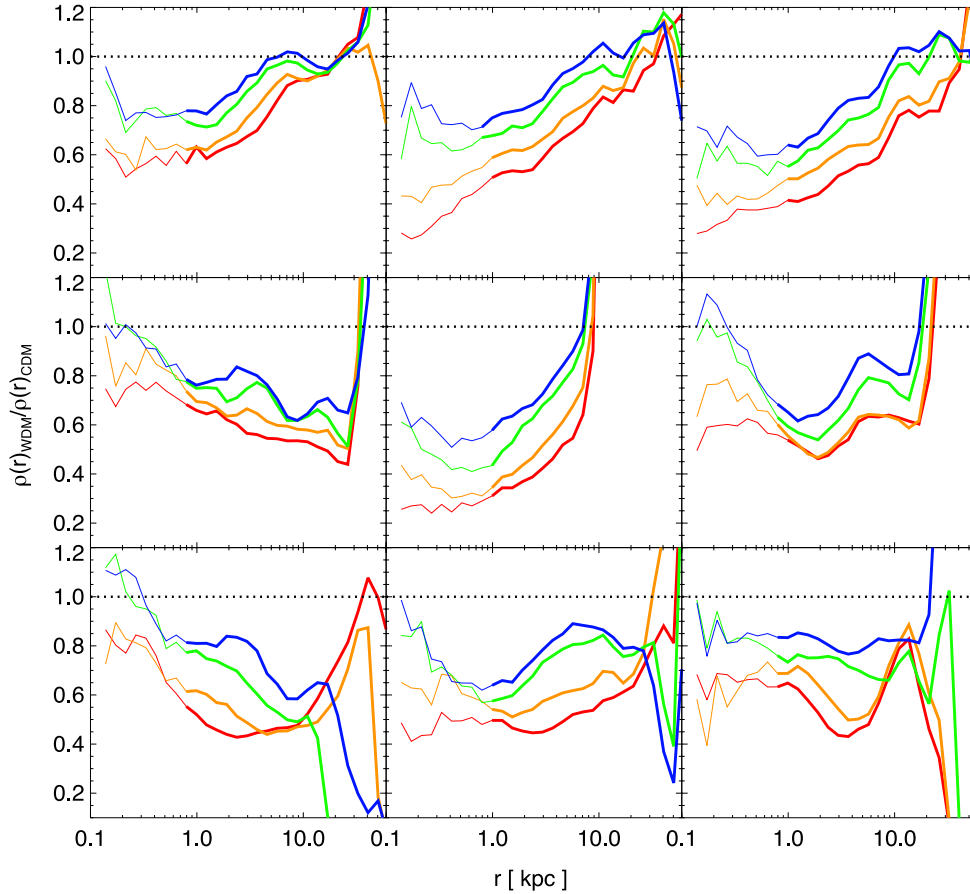


**Figure 18.** Ratio of the density profiles of matched subhaloes in simulations of different WDM particle mass relative to the mass of the CDM counterpart. The colours are as in Fig. 17 as is the use of thick and thin lines.

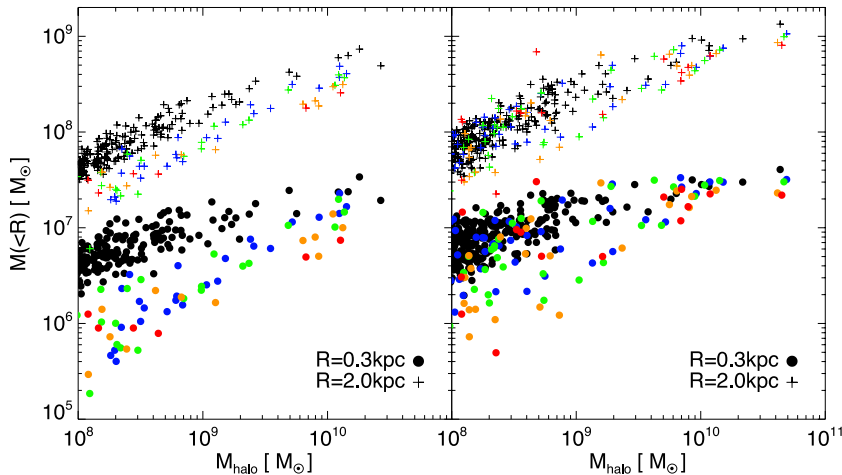


**Figure 19.** Central masses of field haloes (left) and subhaloes within  $r_{200b}$  (right), evaluated within radii of 2 kpc (crosses) and 300 pc (circles) as a function of total mass. Different colours correspond to different simulations: black for CDM-W7, blue, green, orange and red for models  $m_{2.3}$ ,  $m_{2.0}$ ,  $m_{1.6}$  and  $m_{1.5}$ , respectively.

#### 4.4 The abundance of the most massive subhaloes

Boylan-Kolchin et al. (2011, 2012) showed that the most massive subhaloes in the Aquarius halo simulations are much too massive and concentrated to host the brightest dSph satellites of the Milky Way. Parry et al. (2012) reached the same conclusion using gas dynamic simulations of the Aquarius haloes. This discrepancy was

called the ‘too big to fail problem’ by Boylan-Kolchin et al. Subsequently Wang et al. (2012) showed that the extent of the discrepancy depends strongly on the mass of the Galactic halo and all but disappears if the Milky Way’s halo has a mass of  $1 \times 10^{12} M_{\odot}$ . Alternatively, Lovell et al. (2012) showed the problem is naturally solved in a WDM model even if the mass of the Galactic halo is  $2 \times 10^{12} M_{\odot}$ . Their WDM model, chosen to have a particle mass

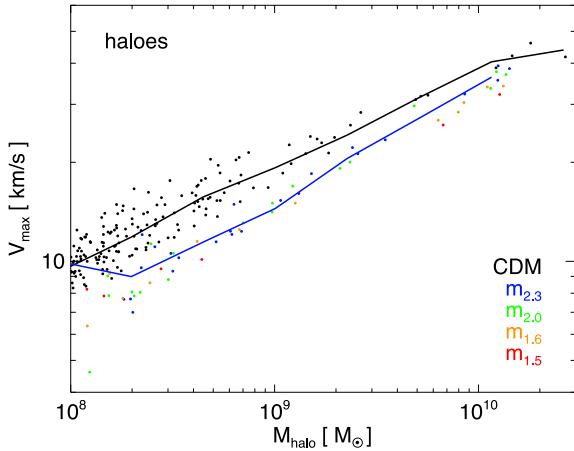


**Figure 20.**  $M_{\text{halo}}$  versus  $V_{\text{max}}$  for field haloes. The black dots show the data for the CDM-W7 simulation and the black line represents the mean relation. The colour dots show data for the WDM simulations: blue, green, orange and red for models  $m_{2.3}$ ,  $m_{2.0}$ ,  $m_{1.6}$  and  $m_{1.5}$ , respectively. The mean relation is shown only for the  $m_{2.3}$  WDM model in which the number of subhaloes is largest and thus the least noisy.

only just compatible with the Lyman  $\alpha$  constraints of Boyarsky et al. (2009a, 2009c) (but not with the more recent constraint quoted by Viel et al. 2013) is the  $m_{1.5}$  model of the current study.

The Milky Way contains three satellites, the LMC, SMC and Sagittarius, that are brighter than the brightest dSph, Fornax. The ‘too big to fail problem’ consists of having substantially more than three massive subhaloes within 300 kpc in the simulations whose properties are incompatible with the measured kinematics of the nine brightest dSphs, specifically with the measured masses within their half-light radii (where masses can be robustly measured from the data; Walker et al. 2009; Wolf et al. 2010). In our WDM simulations we thus count the number of subhaloes within 300 kpc of the main halo centre that have circular velocity profiles of amplitude greater than the measured half-light circular velocities of the nine brightest dSphs plus their  $3\sigma$  errors (Walker et al. 2009; Wolf et al. 2010; Lovell et al. 2012). We find 1, 1, 3 and 4 subhaloes in the  $m_{1.5}$ ,  $m_{1.6}$ ,  $m_{2.0}$  and  $m_{2.3}$  WDM models, respectively, and 6 in CDM-W7. Thus, all our WDM simulations are free of the ‘too big to fail problem’ even in a  $2 \times 10^{12} M_{\odot}$  Galactic halo. Note that if we knew the mass of the Milky Way halo precisely, this argument could, in principle, be used to set an *upper limit* on the (thermal) WDM particle mass.

## 5 DISCUSSION AND CONCLUSIONS

Although the existence of dark matter was inferred in the 1930s, its identity remains one of the most fundamental unsolved questions in physics. The evidence points towards dark matter being made of as yet undiscovered elementary particles. Over the past 30 years attention has focused on CDM (Peebles 1982; Davis et al. 1985; Bardeen et al. 1986) but this is not the only possibility. For example, the lightest sterile neutrino in the  $\nu$ MSM model (Asaka & Shaposhnikov 2005) would behave as WDM, generating very similar structures to CDM on scales larger than bright galaxies but very different structures on smaller scales (Lovell et al. 2012; Macciò et al. 2012; Schneider et al. 2012).

In this study we have carried out a series of high resolution  $N$ -body simulations of galactic haloes in universes dominated by WDM, taking as the starting point one of the haloes from the Aquarius

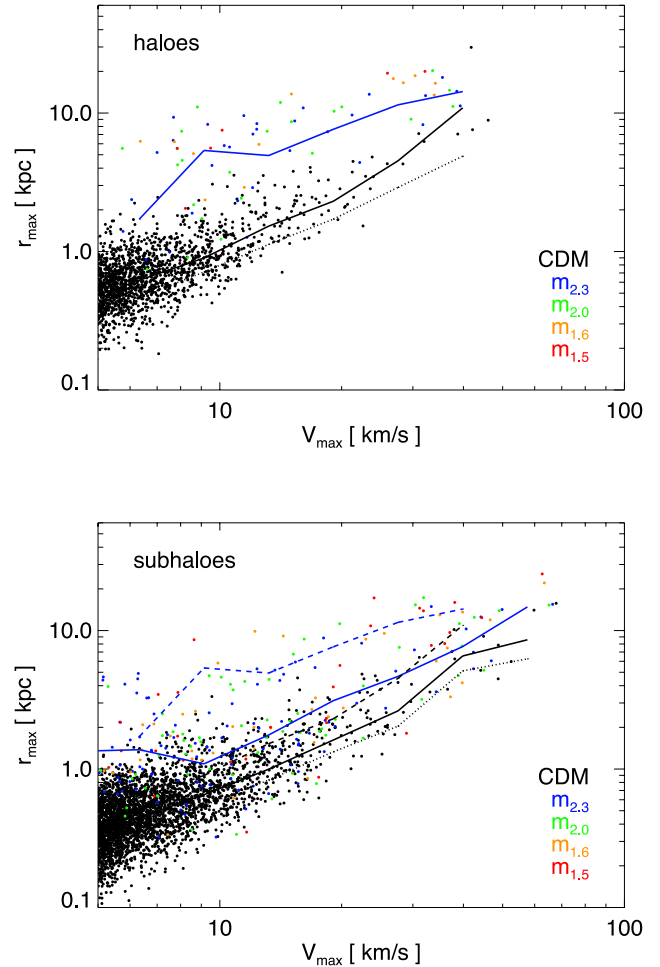


**Figure 21.**  $V_{\text{max}}$  versus  $r_{\text{max}}$  for independent haloes (top) and subhaloes (bottom). The black dots show the data for the CDM-W7 simulation and the black line represents the mean relation in the case. The dotted line corresponds to a  $\Lambda$ CDM simulation using the *WMAP1* cosmological parameters. The colour dots show data for the WDM simulations: blue, green, orange and red for models  $m_{2.3}$ ,  $m_{2.0}$ ,  $m_{1.6}$  and  $m_{1.5}$ , respectively. The mean relation is shown only for the  $m_{2.3}$  WDM model in which the number of subhaloes is largest and thus the least noisy. The solid lines of the top panel are reproduced in the bottom panel as dashed lines.

project of simulations of CDM galactic haloes carried out by the Virgo Consortium (‘Aq-A’ in Springel et al. 2008a). As a prelude we resimulated this CDM halo replacing the cosmological parameters from the *WMAP* year-1 values assumed by Springel et al. to the *WMAP* year-7 values (Komatsu et al. 2011). For CDM this change has the effect of lowering the central densities of galactic subhaloes, alleviating (but not eliminating) the tension between the structure of CDM subhaloes orbiting in haloes of mass  $\sim 2 \times 10^{12} M_{\odot}$  and the kinematical data for Milky Way satellites (Boylan-Kolchin et al. 2012; Wang et al. 2012). We then performed a series of simulations of WDM haloes, using as initial conditions the same fluctuation phases and linear power spectrum of Aq-A, suitably truncated to represent WDM with (thermal equivalent) particle masses in the range 1.5 to 2.3 keV. Our main simulations correspond to level-2 resolution in the notation of Springel et al. (2008a), but we also ran simulations at lower resolution to establish convergence.

$N$ -body simulations with a resolved cutoff in the initial power spectrum undergo artificial fragmentation in filaments (Bode et al. 2001; Wang & White 2007). The resulting spurious structures need

to be identified before the simulations can be analysed. This is best done in the initial conditions: we found that the spurious fragments evolve from disc-like structures that are much flatter than the progenitors of genuine haloes. The sphericity of structures in the initial conditions therefore provides a robust flag for spurious objects which we supplement with a mass cut,  $M_{\min}$ , derived from the limiting mass for genuine haloes,  $M_{\text{lim}}$ , inferred by Wang & White (2007) from simulations of HDM models. We find that a cut of  $M_{\min} = \kappa M_{\text{lim}}$ , with  $\kappa = 0.5$ , captures the results from a comparison of matched haloes in simulations of different resolution. The combined sphericity and mass cut criteria result in clean catalogues of genuine haloes and subhaloes.

The spherically averaged density profile of the main halo is virtually indistinguishable in the CDM and all our WDM simulations but there are large differences in the abundance and structure of their subhaloes. For WDM, the subhalo mass functions begin to diverge from the CDM case at masses between  $\sim 2 \times 10^9 M_{\odot}$  for the  $m_{2.3}$  (least extreme) and  $\sim 7 \times 10^9 M_{\odot}$  for the  $m_{1.5}$  (most extreme) models. The cumulative mass functions are well fitted by fitting functions given in Section 4.1: they become essentially flat for subhaloes masses below  $\sim 7 \times 10^9 M_{\odot}$ . The mass fraction in substructures within  $r_{200b}$  is lower than in the CDM case by factors between 2.4 (for  $m_{1.5}$ ) and 2 (for  $m_{2.3}$ ). The radial distributions of subhaloes are very similar to the CDM case.

WDM haloes and subhaloes are cuspy (except in the very inner regions – see Macciò et al. 2012; Shao et al. 2013) and are well fitted by NFW profiles, and even better by Einasto profiles. However, the central density of WDM haloes depends on the WDM particle mass: in those cases where it is possible to identify the same subhalo in CDM and different WDM simulations, the density profiles have systematically shallower slopes in the latter which become flatter for smaller particle masses. This change of slope is reflected in the main halo mass,  $M_{\text{host}} - M_{\text{sub}}$ ,  $M_{\text{sub}} - V_{\text{max}}$  and  $V_{\text{max}} - r_{\text{max}}$  relations, such that, for a given mass, subhaloes in warmer dark matter models have progressively lower central densities, lower values of  $V_{\text{max}}$  and higher values of  $r_{\text{max}}$  relative to CDM subhaloes. These differences affect the evolution of subhaloes once they fall into the main halo since less concentrated haloes are more easily stripped.

Both the abundance and the structure of WDM subhaloes can be compared to observational data. The requirement that the models should produce at least as many subhaloes as there are observed satellites in the Milky Way sets a lower limit to the WDM particle mass. This is a very conservative limit since feedback processes, arising from the reionization of gas in the early universe and supernova energy, would prevent the formation of galaxies in small mass haloes just as they do in CDM models (e.g. Benson et al. 2002). However, the number of subhaloes above a given mass or  $V_{\text{max}}$  depends, of course, on the host halo mass (Gao et al. 2004; Wang et al. 2012). For the case we have considered, in which  $M_{\text{host}} \sim 10^{12} M_{\odot}$ , we find that the WDM particle mass must be greater than 1.5 or 1.6 keV depending on whether we simply consider the observed number of satellites or apply a correction for the limited area surveyed by the SDSS. This limit is less stringent than that limit of 3.3 keV ( $2\sigma$ ) inferred by Viel et al. (2013) from the clumpiness of the Lyman  $\alpha$  forest of a sample of quasars at redshift  $z > 4$ , although the two results are not directly comparable because Viel et al. (2013) use a slightly different transfer function. In principle, it might also be possible to set an upper limit on the WDM particle mass by comparing the subhalo central densities with those inferred for the brightest satellites of galaxies like the Milky Way. Current kinematical data are insufficient for this test but they are compatible with the properties of the most massive subhaloes in the four WDM

models we have considered none of which suffers from the ‘too big to fail’ problem highlighted by Boylan-Kolchin et al. (2012).

WDM remains a viable alternative to CDM, alongwith other possibilities such as self-interacting dark matter (Vogelsberger et al. 2012) and cold-plus-warm mixtures (Anderhalden et al. 2013). Further theoretical work, including simulations and semi-analytical calculations (Benson et al. 2013; Kennedy et al. 2013) combined with better data for dwarf galaxies offer the prospect of ruling out or validating these models.

## ACKNOWLEDGEMENTS

MRL acknowledges an STFC studentship (STFC grant reference ST/F007299/1). CSF acknowledges ERC Advanced Investigator grant COSMIWAY. We would like to thank the anonymous referee for a careful reading of the text. The simulations used in this paper were carried out on the Cosmology Machine supercomputer at the Institute for Computational Cosmology, Durham. LG acknowledges support from the One hundred talents Programme of the Chinese Academy of Science (CAS), the National Basic Research Programme of China (programme 973, under grant no. 2009CB24901), NSFC grant no. 10973018 and an STFC Advanced Fellowship. This work used the DiRAC Data Centric system at Durham University, operated by the Institute for Computational Cosmology on behalf of the STFC DiRAC HPC Facility ([www.dirac.ac.uk](http://www.dirac.ac.uk)). This equipment was funded by BIS National E-infrastructure capital grant ST/K00042X/1, STFC capital grant ST/H008519/1, and STFC DiRAC Operations grant ST/K003267/1 and Durham University. DiRAC is part of the National E-Infrastructure. This work was supported in part by an STFC rolling grant to the ICC. The data featured in the figures in this paper are available on request from MRL.

## REFERENCES

- Anderhalden D., Schneider A., Macciò A. V., Diemand J., Bertone G., 2013, *J. Cosmol. Astropart. Phys.*, 3, 14  
 Angulo R. E., Hahn O., Abel T., 2013, *MNRAS*, 434, 337  
 Asaka T., Shaposhnikov M., 2005, *Phys. Lett. B*, 620, 17  
 Avila-Reese V., Colín P., Valenzuela O., D’Onghia E., Firmani C., 2001, *ApJ*, 559, 516  
 Bardeen J. M., Bond J. R., Kaiser N., Szalay A. S., 1986, *ApJ*, 304, 15  
 Bell E. F., Slater C. T., Martin N. F., 2011, *ApJ*, 742, L15  
 Benson A. J., Frenk C. S., Lacey C. G., Baugh C. M., Cole S., 2002, *MNRAS*, 333, 177  
 Benson A. J. et al., 2013, *MNRAS*, 428, 1774  
 Bode P., Ostriker J. P., Turok N., 2001, *ApJ*, 556, 93  
 Boyarsky A., Lesgourgues J., Ruchayskiy O., Viel M., 2009a, *J. Cosmol. Astropart. Phys.*, 5, 12  
 Boyarsky A., Ruchayskiy O., Shaposhnikov M., 2009b, *Ann. Rev. Nucl. Part. Sci.*, 59, 191  
 Boyarsky A., Lesgourgues J., Ruchayskiy O., Viel M., 2009c, *Phys. Rev. Lett.*, 102, 201304  
 Boyarsky A., Iakubovskiy D., Ruchayskiy O., 2012, *Phys. Dark Univ.*, 1, 136  
 Boylan-Kolchin M., Springel V., White S. D. M., Jenkins A., 2010, *MNRAS*, 406, 896  
 Boylan-Kolchin M., Bullock J. S., Kaplinghat M., 2011, *MNRAS*, 415, L40  
 Boylan-Kolchin M., Bullock J. S., Kaplinghat M., 2012, *MNRAS*, 422, 1203  
 Brooks A. M., Zolotov A., 2012, preprint ([arXiv:e-prints](https://arxiv.org/abs/1203.4015))  
 Bullock J. S., Kravtsov A. V., Weinberg D. H., 2000, *ApJ*, 539, 517  
 Cole S. et al., 2005, *MNRAS*, 362, 505  
 Colín P., Valenzuela O., Avila-Reese V., 2008, *ApJ*, 673, 203  
 Davis M., Efstathiou G., Frenk C. S., White S. D. M., 1985, *ApJ*, 292, 371  
 de Vega H. J., Sanchez N. G., 2010, *MNRAS*, 404, 885



- di Cintio A., Knebe A., Libeskind N. I., Yepes G., Gottlöber S., Hoffman Y., 2011, *MNRAS*, 417, L74
- Diemand J., Moore B., Stadel J., 2005, *Nature*, 433, 389
- Einasto J., 1965, *Tr. Astrofiz. Inst. Alma-Ata*, 5, 87
- Ellis J., Hagelin J. S., Nanopoulos D. V., Olive K., Srednicki M., 1984, *Nucl. Phys. B*, 238, 453
- Frenk C. S., White S. D. M., 2012, *Ann. Phys.*, 524, 507
- Gao L., White S. D. M., Jenkins A., Stoehr F., Springel V., 2004, *MNRAS*, 355, 819
- Gilmore G., Wilkinson M. I., Wyse R. F. G., Kleya J. T., Koch A., Evans N. W., Grebel E. K., 2007, *ApJ*, 663, 948
- Hahn O., Abel T., Kaehler R., 2012, *MNRAS*, 434, 1171
- Hogan C. J., Dalcanton J. J., 2000, *Phys. Rev. D*, 62, 063511
- Ibata R., Martin N. F., Irwin M., Chapman S., Ferguson A. M. N., Lewis G. F., McConnachie A. W., 2007, *ApJ*, 671, 1591
- Kaiser N. et al., 2010, *Proc. SPIE*, 7733, 77330E
- Kamada A., Yoshida N., Kohri K., Takahashi T., 2013, *J. Cosmol. Astropart. Phys.*, 3, 8
- Kennedy R., Frenk C., Cole S., Benson A., 2013, preprint ([arXiv:e-prints](https://arxiv.org/abs/1308.4002))
- Knebe A., Devriendt J. E. G., Mahmood A., Silk J., 2002, *MNRAS*, 329, 813
- Komatsu E. et al., 2011, *ApJS*, 192, 18
- Koposov S. et al., 2008, *ApJ*, 686, 279
- Kusenko A., 2009, *Phys. Rep.*, 481, 1
- Larson D. et al., 2011, *ApJS*, 192, 16
- Libeskind N. I., Frenk C. S., Cole S., Helly J. C., Jenkins A., Navarro J. F., Power C., 2005, *MNRAS*, 363, 146
- Lovell M. R. et al., 2012, *MNRAS*, 420, 2318
- Macciò A. V., Paduouiu S., Anderhalden D., Schneider A., Moore B., 2012, *MNRAS*, 424, 1105
- Macciò A. V., Paduouiu S., Anderhalden D., Schneider A., Moore B., 2013, *MNRAS*, 428, 3715
- Martin N. F. et al., 2009, *ApJ*, 705, 758
- Martin N. F. et al., 2013, *ApJ*, 772, 15
- Navarro J. F., Eke V. R., Frenk C. S., 1996a, *MNRAS*, 283, L72
- Navarro J. F., Frenk C. S., White S. D. M., 1996b, *ApJ*, 462, 563
- Navarro J. F., Frenk C. S., White S. D. M., 1997, *ApJ*, 490, 493
- Navarro J. F. et al., 2004, *MNRAS*, 349, 1039
- Okamoto T., Frenk C. S., Jenkins A., Theuns T., 2010, *MNRAS*, 406, 208
- Papastergis E., Martin A. M., Giovanelli R., Haynes M. P., 2011, *ApJ*, 739, 38
- Parry O. H., Eke V. R., Frenk C. S., Okamoto T., 2012, *MNRAS*, 419, 3304
- Peebles P. J. E., 1982, *ApJ*, 263, L1
- Peñarrubia J., McConnachie A. W., Navarro J. F., 2008, *ApJ*, 672, 904
- Polisensky E., Ricotti M., 2011, *Phys. Rev. D*, 83, 043506
- Pontzen A., Governato F., 2012, *MNRAS*, 421, 3464
- Power C., Navarro J. F., Jenkins A., Frenk C. S., White S. D. M., Springel V., Stadel J., Quinn T., 2003, *MNRAS*, 338, 14
- Preskill J., Wise M. B., Wilczek F., 1983, *Phys. Lett. B*, 120, 127
- Sawala T., Frenk C. S., Crain R. A., Jenkins A., Schaye J., Theuns T., Zavala J., 2013, *MNRAS*, 431, 1366
- Schneider A., Smith R. E., Macciò A. V., Moore B., 2012, *MNRAS*, 424, 684
- Shandarin S., Habib S., Heitmann K., 2012, *Phys. Rev. D*, 85, 083005
- Shao S., Gao L., Theuns T., Frenk C. S., 2013, *MNRAS*, 430, 2346
- Somerville R. S., 2002, *ApJ*, 572, L23
- Springel V., White S. D. M., Tormen G., Kauffmann G., 2001, *MNRAS*, 328, 726
- Springel V. et al., 2005, *Nature*, 435, 629
- Springel V. et al., 2008a, *MNRAS*, 391, 1685
- Springel V. et al., 2008b, *Nature*, 456, 73
- Strigari L. E., Frenk C. S., White S. D. M., 2010, *MNRAS*, 408, 2364
- Tikhonov A. V., Gottlöber S., Yepes G., Hoffman Y., 2009, *MNRAS*, 399, 1611
- Tollerud E. J., Bullock J. S., Strigari L. E., Willman B., 2008, *ApJ*, 688, 277
- Tollerud E. J. et al., 2012, *ApJ*, 752, 45
- Vera-Ciro C. A., Helmi A., Starkenburg E., Breddels M. A., 2013, *MNRAS*, 428, 1696
- Viel M., Lesgourgues J., Haehnelt M. G., Matarrese S., Riotto A., 2005, *Phys. Rev. D*, 71, 063534
- Viel M., Becker G. D., Bolton J. S., Haehnelt M. G., 2013, *Phys. Rev. D*, 88, 043502
- Vogelsberger M., Zavala J., Loeb A., 2012, *MNRAS*, 424, 2715
- Wadepuhl M., Springel V., 2011, *MNRAS*, 410, 1975
- Walker M. G., Mateo M., Olszewski E. W., Peñarrubia J., Wyn Evans N., Gilmore G., 2009, *ApJ*, 704, 1274
- Walker M. G., Mateo M., Olszewski E. W., Peñarrubia J., Wyn Evans N., Gilmore G., 2010, *ApJ*, 710, 886
- Walsh S. M., Jerjen H., Willman B., 2007, *ApJ*, 662, L83
- Wang J., White S. D. M., 2007, *MNRAS*, 380, 93
- Wang J., Frenk C. S., Navarro J. F., Gao L., Sawala T., 2012, *MNRAS*, 424, 2715
- White S. D. M., 1994, preprint ([arXiv:e-prints](https://arxiv.org/abs/199405014))
- Willman B. et al., 2005, *ApJ*, 626, L85
- Wolf J., Martinez G. D., Bullock J. S., Kaplinghat M., Geha M., Muñoz R. R., Simon J. D., Avedo F. F., 2010, *MNRAS*, 406, 1220
- York D. G. et al., 2000, *AJ*, 120, 1579
- Zavala J., Okamoto T., Frenk C. S., 2008, *MNRAS*, 387, 364
- Zolotov A. et al., 2012, *ApJ*, 761, 71

## APPENDIX A: CONVERGENCE STUDY

For several dSph satellites of the Milky Way it is possible to measure the circular velocity at the radius encompassing half the light in a relatively model-independent way (Walker et al. 2009; Wolf et al. 2010). The smallest measured value is  $5.7 \text{ km s}^{-1}$  for Leo IV. The circular velocity at the half-light radius is a lower bound on  $V_{\text{max}}$ . Therefore, to compare with Milky Way data, we need the number of subhaloes in the simulations with  $V_{\text{max}}$  greater than  $5.7 \text{ km s}^{-1}$ . It is important to check that the simulations resolve all these subhaloes.

We have performed a convergence study using the levels 4, 3 and 2 simulations for two of the WDM models. For the  $m_{2.3}$  model, the subhalo  $V_{\text{max}}$  function at level 4 deviates by 10 per cent from that in the corresponding level 2 simulation at a value of  $V_{\text{max}} = 11 \text{ km s}^{-1}$ ; the level 3 subhalo  $V_{\text{max}}$  function deviates by the same amount at a value of  $V_{\text{max}} = 6 \text{ km s}^{-1}$ . The particle masses in the levels 4 and 3 simulations differ by a factor of 8. If we write  $(m_4/m_3)^n = V_{\text{max}}(4)/V_{\text{max}}(3)$  (where the numbers denote the resolution level) we find  $n = 0.29$ . The high resolution, level 2, simulation has a particle mass 3.6 times smaller than that of level 3. Therefore, we expect this simulation to be complete to 10 per cent at  $V_{\text{max}} = 4.2 \text{ km s}^{-1}$ . A similar analysis for the  $m_{1.5}$  simulation shows that this is already complete at level 3 for  $V_{\text{max}} = 5.7 \text{ km s}^{-1}$ .

We have checked the validity of this approach by analysing the original Aquarius Aq-A2 and Aq-A1 simulations. The Aq-A1 simulation has a particle mass of  $1.7 \times 10^3 M_{\odot}$ , a factor of  $\sim 8$  smaller than the level 2 simulations. We find that at  $V_{\text{max}} = 5.7 \text{ km s}^{-1}$  the Aq-A2 subhalo  $V_{\text{max}}$  function deviates by 8 per cent from the Aq-A1 result. The suppression of small subhaloes in WDM models should result in better subhalo completeness in this case compared to CDM in this mass range (cf. convergence between levels 3 and 2 for  $m_{1.5}$ ). We therefore conclude that we have lost no more than 8 per cent of the ‘true’ number of subhaloes in the  $m_{2.3}$  simulation and even fewer in the warmer models.

This paper has been typeset from a  $\text{\TeX}/\text{\LaTeX}$  file prepared by the author.